7-2019

Major and Trace Element Analyses for Studying Oceanic Crustal Construction and Ridge Morphology Along the Kane- Atlantis Supersegment of the Mid-Atlantic Ridge

Yitong Lyu
University of Nebraska - Lincoln, ylv2@unl.edu

MAJOR AND TRACE ELEMENT ANALYSES FOR STUDYING OCEANIC CRUSTAL CONSTRUCTION AND RIDGE MORPHOLOGY ALONG THE KANE- ATLANTIS SUPERSEGMENT OF THE MID-ATLANTIC RIDGE

by

Yitong Lyu

A THESIS

Presented to the Faculty of

The Graduate College at the University of Nebraska

In Partial Fulfillment of Requirements

For the Degree of Master of Science

Major: Earth and Atmospheric Sciences

Under the Supervision of Professor Lynne J. Elkins

Lincoln, Nebraska

July, 2019

MAJOR AND TRACE ELEMENT ANALYSES FOR STUDYING OCEANIC CRUSTAL CONSTRUCTION AND RIDGE MORPHOLOGY ALONG THE KANE- ATLANTIS SUPERSEGMENT OF THE MID-ATLANTIS RIDGE

Yitong Lyu, M.S

University of Nebraska, 2019

Advisor: Lynne J. Elkins

Faulting style along slow-spreading ridge segments exerts a major control over oceanic crustal construction and ridge morphology. Seafloor spreading along slow-spreading ridges is classified into asymmetrical detachment faulting and symmetrical spreading styles. Magma supply variations may influence the formation of symmetric versus asymmetric segments, but the factors that derive such variations remain unclear. We present U and Th concentration data by isotope dilution for basalts from 24 to 30 ^{o}N MAR, of which 18 samples were retrieved from detachment faulted and 10 from symmetrical segments. The U-Th concentration results from this study are further compiled with prior published data from Gale et al. (2013) and data from Langmuir (personal communication). The compiled dataset provides robust combined major and trace element analyses of basalts from the study area.

Statistical analyses show that basalt samples from asymmetrical segments have higher mean MgO, but lower mean Na_2O, Sr and Sr/Nd contents compared to samples from

symmetrical segments (at the 95% confidence level). The differences in these major and trace elements may indicate a higher proportion of pyroxenites and/or a more trace element enriched peridotite in the source mantle beneath symmetrical segments, which increases the magma supply and prevents the formation of detachment faults beneath these segments. Furthermore, the larger amount of magma supply facilitates the crust to fully accommodate seafloor spreading and generate symmetrical accretion along the Kane-Atlantis segments. On the other hand, the detachment faults beneath asymmetrical segments may decrease the degrees of assimilation and fractional crystallization at shallow levels.

Acknowledgement

I would first like to thank my thesis advisor Dr. Lynne J. Elkins of the Department of Earth and Atmospheric Science at the University of Nebraska-Lincoln. Dr. Elkins was always patient and willing to offer me generous help whenever I had troubles or questions about my research or thesis. She insisted on this thesis to be my own work, but always provided valuable suggestions to help me stay in the right direction.

I would also like to thank the rest of my thesis committee: Dr. Caroline Burberry and Dr. Richard Kettler, for generously offering their time and suggestions throughout the preparation and review of this thesis.

I would also like to thank National Science Foundation for funding me to do this project (grant number: OCE-MGG-1658011), as well as the Department of Earth and Atmospheric Science for offering me research assistantship and allowing me to use UNITE lab during the past two years.

My sincere thanks also go to Dr. Kenneth Sims and Lisa B. Kant, who arranged and helped me to do U-Th ICP-MS measurements at the University of Wyoming. I am grateful to Dr. Charles Langmuir, who shared his elemental measurements with me.

Finally, I want to thank my parents for providing me with endless support, love and encouragement throughout my years of study. This thesis would not have been finished without them.

Yitong Lyu

List of Tables

List of Figures

1. Introduction

Mid-ocean ridge basalts (MORB) are principally the products of magmas that erupted along mid-ocean ridges (e.g., Klein and Langmuir, 1987; Johnson and Dick, 1992; Kinzler, 2006; Asimow, 2001; Ito and Mahoney, 2005; Niu and Batiza, 1997; Hofmann, 2014). Studying mid-ocean ridge crustal construction provides opportunities to better model the movements of magmas beneath mid-ocean ridges, which helps to develop our understanding of key relationships between mantle dynamics and the generation of new ocean crust. However, there is still not a uniform consensus about what dominantly governs magma transport and oceanic crust construction. A considerable amount of relevant literature has been published over the past decade, which focused on studying the relationship between crustal construction mechanisms and their determinants (e.g., Klein and Langmuir, 1987, 1989; White and Klein, 2013; Bourdon et al., 1996; Elkins et al., 2014, 2016; Petermann and Hirschmann, 2002; Standish et al., 2008; Fujii and Scarfe, 1985; Dupré and Allègre, 1983; Plank and Langmuir, 2008; Lee and Chin, 2014; Hofmann, 2003; Langmuir and Hanson, 1980; Claude-Ivanaj et al., 2001; Dungan and Rhodes, 1978; Wilson et al., 2013; Prytulak and Elliott, 2009; Pietruszka et al., 2013; McKenzie et al., 2004; Kogiso et al., 2004; Dick et al., 1984; Hofmann, 1997; Hirschmann and Stolper, 1996; Rudge et al., 2013). Many of these works emphasize connecting MORB genesis with a single factor (such as mantle temperature, mantle source heterogeneity, or melting regime). For example, Klein and Langmuir (1987) stated that mantle source temperature principally controls the extent of melting and the thickness of the crust;

while Niu and Batiza (1997) demonstrated that the mantle source of the East Pacific Rise (EPR) is heterogeneous on very small scales from trace element analyses. Despite the fact that some researchers consider the influences of multiple factors on the final composition of MORB (e.g., Standish et al., 2008; Komiya et al., 2004, 2002; Dick and Zhou, 2014; Woodhead, 1989; Haase, 2002; Niu et al., 2002), few of them consider the relationships between these indicators and faulting styles at these ridge segments. Coupled major and trace element analyses are powerful tools because some of these elements and their ratios (such as Mg, Fe, Al, Th, U) show enrichment or depletion signals when a specific lithology exists in the source or the extent of melting changes (Klein and Langmuir, 1987; Stracke and Bourdon, 2009). Therefore, comprehensive major and trace element analyses help to answer questions such as how to distinguish the major and trace element signatures from source heterogeneity or the melting process; and if mantle temperature, mantle heterogeneity and the melting process all control melting, which factor is the primary determinant.

The Mid-Atlantic Ridge (MAR), which is a typical slow-spreading ridge system, provides an ideal study region. Slow-spreading ridges (i.e., ridges with half-spreading rates less than 18 mm/yr; Murton and Rona, 2015) account for 80% of the total length of the global mid-ocean ridge system (Murton and Rona, 2015). Studying the MAR helps us to identify and characterize the major controls on magma transport mechanisms at slow-spreading ridges and contribute to models of global crustal construction at all spreading rates. Furthermore, slow-spreading ridges are the major

hosts of detachment faults (Yu et al., 2013). Studies show that detachment faults may play a central role in controlling magma supply and crustal accretion modes, which consequently affect MORB composition and seafloor morphology (Murton and Rona, 2015; Smith et al., 2008; Escartín et al., 2008). Several hydrothermal fields and oceanic core complexes (OCCs, which refer to gabbroic rock exposures on the seafloor; Ildefonse et al., 2007) along the MAR have been identified, and studies have demonstrated that their formation is closely associated with the presence of detachment faults (e.g., Cherkashov et al., 2008; Kelley et al., 2001; Kransnov et al., 1994; German et al., 1996; Humphris et al., 2015; Rona et al., 1984; Ildefonse et al., 2007; Canales, 2010; Escartín et al., 2008; Canales et al., 2007; Boschi et al., 2006; Smith et al., 2006; Planert et al., 2010). This helps us identify detachment faulted segments and their compositional and lithological characteristics. Since MORB reflect compositions of the source rock, chemical variations of basalts from different segments may reveal the relationship between source heterogeneity, magma supply variations and slow-spreading ridge morphology.

This study focuses on the Kane-Atlantis supersegment of 24-30^{o}N MAR (Fig. 1,Table 1) and offers a comprehensive discussion by reporting high precision trace element U and Th concentration measurements of 34 basaltic samples from the entire study area, and comparing the results with prior published major and trace element data from the same area. Here I aim to (1) characterize the chemical compositions of samples from both symmetrical and asymmetrical segments; (2) differentiate mantle source related geochemical signatures from partial melting

related signatures; (3) compare the relative roles of mantle source heterogeneity, extent of melting, and melt mixing in determining the final MORB compositions; and (4) assess how and to what extent measures of magma supply correlate with seafloor morphology and faulting style. Comparisons of the contents of MgO, Na_2O, Sr and Sr/Nd in both symmetrical and asymmetrical segment samples indicate that mantle source heterogeneity is the primary determinant of magma supply and ridge morphology at the Kane-Atlantis supersegment.

2. Background

A primary motivation for analyzing MORB is to characterize the major controls on magma supply, which may influence emplacement style at slow-spreading mid-ocean asymmetrical and symmetrical ridges, thereby affecting seafloor morphology. Before proceeding to a detailed discussion about which factors exert a predominant control over crust formation, it is necessary to briefly review the likely major factors and the geologic setting of the Kane-Atlantis supersegment

Table 1. Location information for the samples from the Kane-Atlantis region.

Sample	Segment and type[1]	Latitude (ºN)			Longitude (ºN)			Depth (m)		
		Start	End	Average	Start	End	Average	Start	End	Average
D01-6	S01, DB	29.97	29.98	29.98	42.74	42.74	42.74	4160	3969	4065
D65-2	S01, AB	29.52	29.62	29.57	42.45	42.45	42.45	2969		2969
D2-SG	S01, AB	29.50	29.50	29.50	42.48	42.48	42.48		3040	3040
D58-3	S03, DB	28.76	28.75	28.75	43.49	43.48	43.49	3682	3499	3590
D08-2	S03, DB	28.67	28.67	28.67	43.54	43.53	43.53	3404	3107	3256
D13-SG	S05, DB	28.65	28.69	28.67	43.57	43.57	43.57		3825	3825
D10-2	S04,DB	28.60	28.59	28.60	43.62	43.62	43.62	3684	3678	3681
D61-SG	S03, DB	28.43	28.43	28.43	43.26	43.26	43.26	3535	3380	3458
D11-4	S04, AB	28.38	28.38	28.38	43.73	43.73	43.73	3210	3174	3192
D09-SG	S04, UK	28.37	28.37	28.37	43.36	43.35	43.36		3498	3498
D12-SG	S05, AB	28.13	28.13	28.13	43.50	43.49	43.49		3763	3763
D16-SG	S07, UK	27.62	27.63	27.62	44.15	44.15	44.15	3958	3832	3895
D14-SG	S05, UK	27.55	27.55	27.55	43.60	43.60	43.60		3224	3224
D17-SG	S06, UK	27.48	27.49	27.49	44.19	44.20	44.19	3364	3289	3326
D15-SG	S06, UK	27.42	27.43	27.43	44.59	44.57	44.58		3654	3654
D22-2	S07, DB	26.74	26.75	26.74	44.53	44.54	44.53	3606	3494	3550
D23-1	S06, DB	26.61	26.60	26.61	44.63	44.63	44.63	4170	4089	4130
D26-2-SG	S09, DB	26.23	26.23	26.23	44.78	44.78	44.78	3866	3815	3841
D32-5	S10, DB	25.65	25.64	25.65	45.20	45.21	45.21	3891	3671	3781
D33-1	S11, DB	25.57	25.57	25.57	45.26	45.26	45.26	4295	4204	4250
D32-SG	S10, AB	25.38	25.39	25.39	45.12	45.13	45.13	3903	3683	3793

Table 1 (continued).

Sample	Segment and type	Latitude (°N)			Longitude (°N)			Depth (m)		
		Start	End	Average	Start	End	Average	Start	End	Average
D50-5	S11, DB	25.33	25.34	25.34	45.41	45.41	45.41	3997	3824	3911
D35-SG	S11, AB	25.28	25.29	25.29	45.42	45.42	45.42	3826	3708	3767
D37-2	S11, AB	25.03	25.03	25.03	45.47	45.46	45.47	3569	3570	3569
D42-2	S12,AB	24.77	24.77	24.77	45.90	45.90	45.90	3893	3833	3863
D47-11	S12, DB	24.75	24.75	24.75	45.81	45.80	45.81	4235	3952	4094
D48-3	S12, AB	24.87	24.86	24.87	45.68	45.68	45.68	4057	3800	3928
D46-6	S12, DB	24.58	24.57	24.57	46.11	46.11	46.11	4434	4284	4359
D42-SG	S12, UK	24.46	24.46	24.46	45.54	45.54	45.54	3882	3974	3928
RC03*	S01, DB			29.87			42.79			2929
RC05*	S01, AB			29.67			42.83			3089
RC47*	S07, DB			27.05			44.44			3723
RC67*	S10, DB			25.91			45.04			3872
RC97*	S10, DB			25.78			45.10			3341

* R samples indicate gravity core samples; the rest D samples are dredge samples.

[1] AB and DB represent abyssal hill-bearing (symmetrical) segments and detachment fault-bearing (asymmetrical) segments, respectively.
UK indicates these segments potentially belong to either AB or DB segment type, but the evidence is unclear (Olive and Escartín, 2016).

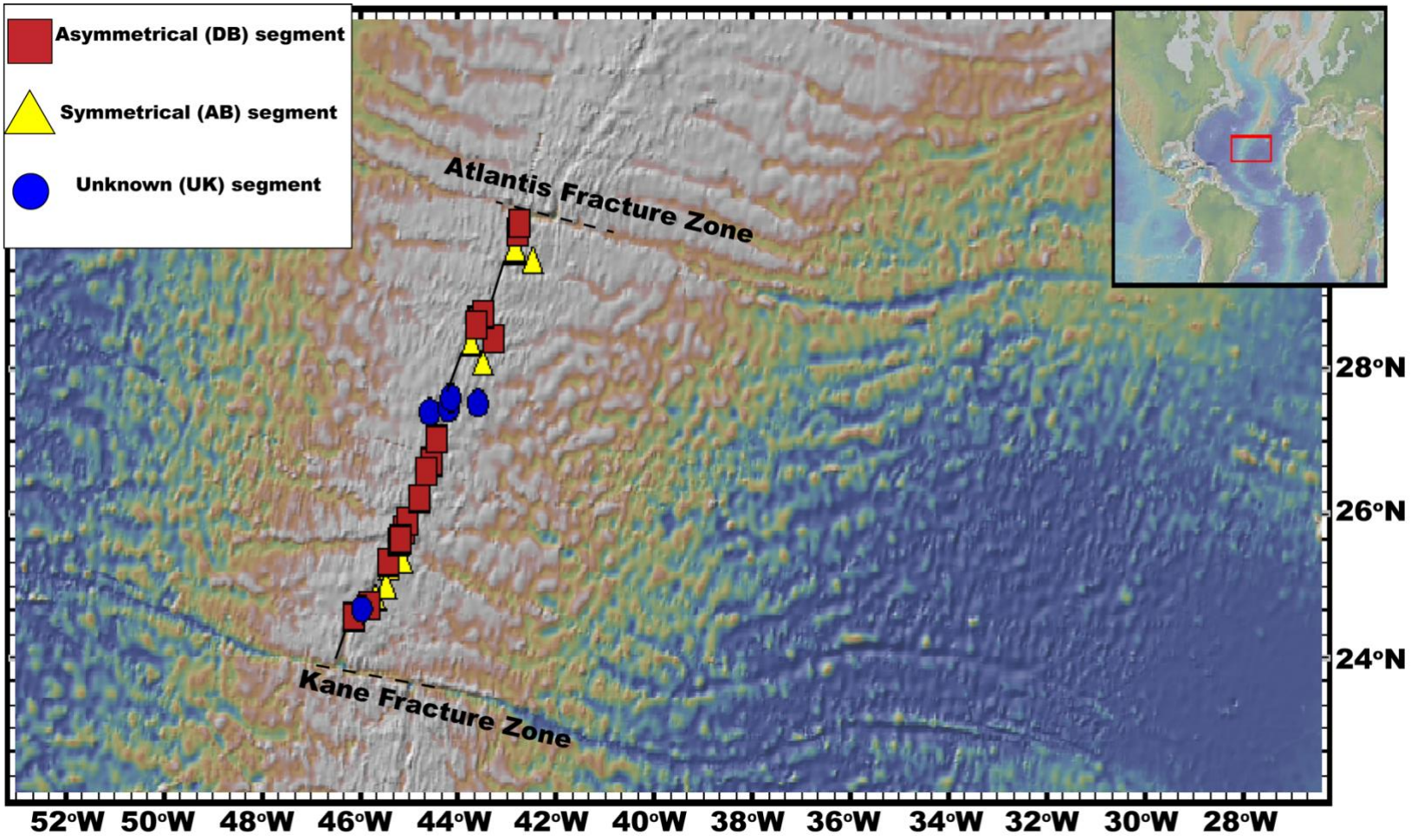

Figure 1. Map of the locations of the basalt samples analyzed in this study with the seafloor bathymetry, after *Sandwell and Smith (2009)*.

2.1 Geologic setting of the Kane-Atlantis supersegment

The study area for this research is the Kane-Atlantis supersegment (24-30^{o}N MAR, Fig. 1), part of the slow-spreading MAR system. Based on the classification of the Kane-Atlantis segment morphology from Olive and Escartín (2016), 18 samples are identified as basalts from detachment fault-bearing (asymmetrical) segments (DB); 10 samples are identified as basalts from abyssal hill-bearing (symmetrical) segments (AB); and the remaining 6 samples are classified as "unknown" (UK) because it is unclear whether these are DB or AB segments. Jin and Zhu (2003) observed that the full spreading rates of the North, Equatorial, and South MAR are 22.3 mm/a, 28.8 mm/a and 30.7 mm/a, respectively. Murton and Rona (2015) reported that the range of axial depths along the Kane-Atlantis supersegment is between 3450-4400m, which gradually increase from Northern to Southern MAR, corresponding to a range of oceanic crustal thickness up to 6km and inferred underlying mantle temperature variations of ~83^{o}C. This observation suggests that mantle temperature is a likely but relatively minor factor influencing crustal construction along the Kane-Atlantis supersegment. The MAR is overall characterized by ~10-20 km wide axial valleys with a series of normal faults, transform faults, and non-transform faults, morphology typical of slow-spreading mid-ocean ridges (Olive and Escartín, 2016; Spencer et al., 1997). Based on mid-ocean ridge segmentation (Murton and Rona, 2015; Macdonald et al., 1988), some second-order ridge segments along the MAR exhibit an

asymmetrical accretion mode and others have a symmetrical accretion mode (Escartín et al., 2008; Murton and Rona, 2015). Besides symmetrical and asymmetrical accretion, oblique spreading segments are also recognized (Abelson and Agnon, 1997). Distinguishing characteristics of asymmetrical and symmetrical accretion matters because the accretion style influences seafloor morphology and hydrothermal activity along the ridge.

Asymmetrical accretion is associated with an active detachment fault along one ridge flank (Humphris et al., 2015b; Smith et al., 2008). Detachment faults underlie likely ~50% of second-order segments along the MAR (Humphris et al., 2015b; Tucholke et al., 2008; MacLeod et al., 2009) and host at least seven of the eleven known active hydrothermal fields on the northern MAR (Tucholke et al., 1998; Tucholke and Lin, 1994). Murton and Rona (2015) identified 13 segments within the Kane-Atlantis supersegment, of which at least 6 are detachment fault bearing. This study further indicates that detachment faults play a critical role in developing the MAR's morphology and lithology, which are also influenced by magma supply and heat extraction (Backer, 2009; Howell et al., 2019). In Fig.2, which illustrates the structure of an asymmetrical ridge segment in cross-section, a single detachment fault is shown to host hydrothermal activity (Escartín et al., 2008). The presence of an active detachment fault beneath the ridge axis causes increased hydrothermal cooling and crustal thickness, and is correlated with decreased magmatic activity. Studies show that low magmatic activity may be a

prerequisite for detachment generation, since a detachment fault will be terminated when magma activity is robust (Humphris et al., 2015a; Tucholke et al., 1998). The thicker lithosphere deepens the top of the melting column beneath asymmetrical segments and decreases the extent of melting. Lissenberg and Dick (2008) indicated that melt-rock reactions beneath detachment faults are high because they are underlain by deep, magma-bearing crystal mush zones. Additionally, the tectonic strain along asymmetrical ridges is high, which results in a high seismicity (Escartín et al., 2008; Müller et al., 2008). To sum up, at asymmetrical segments, the mean extent of melting beneath the ridges is low, the seismic activity is high, and the melt-rock reactions are expected to be robust.

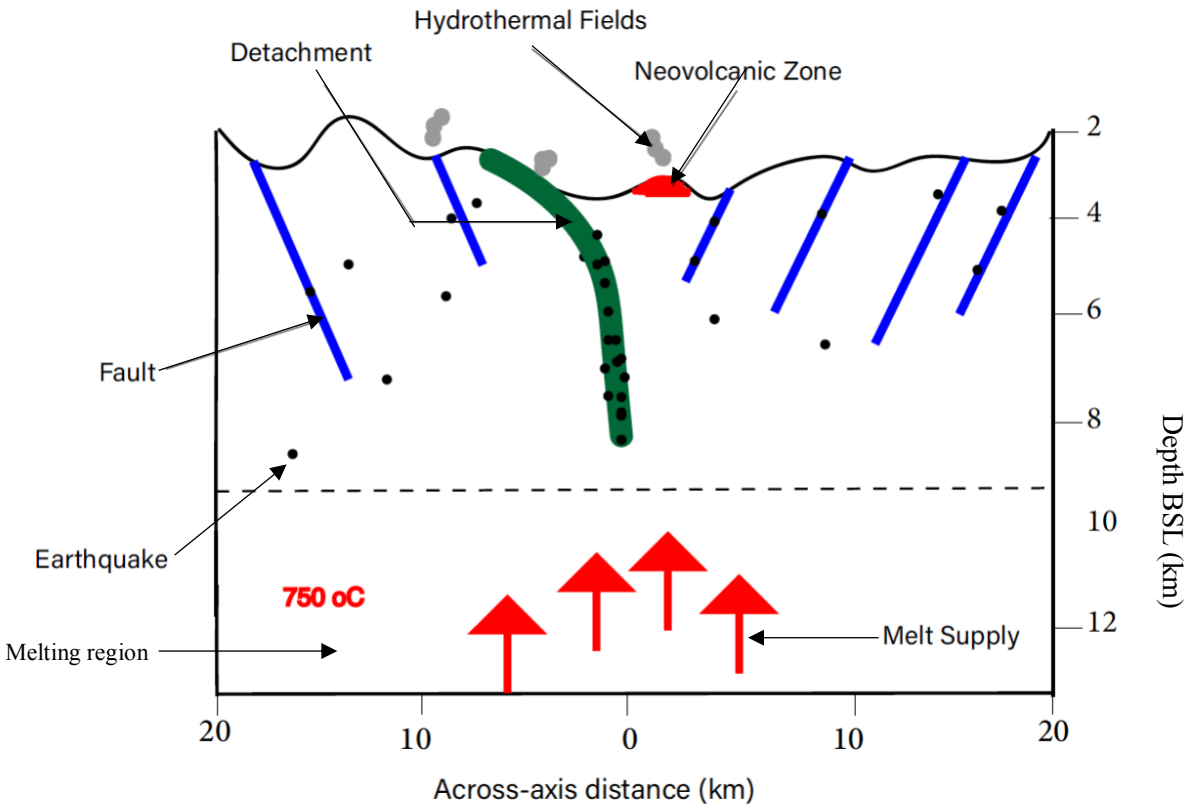

Figure 2. Cross section of a detachment fault-bearing ridge (after *Escartín et al., 2008*). The dashed line

indicates the top of the melting regime with a melting temperature of 750°C. Red arrows indicate ascending magma. In asymmetrical segment systems, the top of the melting regime is low, which results in a low extent of melting and a thick lithosphere.

An example of how detachment faults may influence hydrothermal activity and asymmetrical accretion would be the Trans-Atlantic Geotraverse (TAG) segment located at 26°08'N between the Kane and Atlantis Fracture Zones (Humphris et al., 2015b). Hydrothermal activity in the TAG hydrothermal field has been episodic over the past 140 ka (Canales et al., 2007b). Ideas about what dominantly controls the hydrothermal activity in the TAG field have changed over the past 30 years (e.g., Lister, 1974; Humphris, 2000; Kong et al., 1992).

In early studies, the TAG hydrothermal field was believed to be a magmatically active system. The heat required to drive the hydrothermal activity was thought to be extracted from a mid-crustal melt reservoir during the crustal cooling process, then removed along ridge-parallel faults and cracks (Canales et al., 2007b; Humphris et al., 2015b). However, geophysical data collected over the last decade demonstrate that the TAG hydrothermal field is in fact accommodated on the hanging wall of an active detachment fault (Humphris et al., 2015a; Tivey et al., 2003). A magnetic survey from the TAG segment identified a linear zone of low magnetization that is close to the east wall of the rift valley. The magnetic low is due to crustal stretching caused by 3.9 km of horizontal extension along a normal fault, which is located in the north-eastern part of the TAG field (Tivey et al., 2003). The existence of the detachment fault is also supported by the exposure of gabbros and dikes

found on the seafloor surface (Zonenshain et al., 1989). This discovery illustrates that buried detachment faulting, rather than magmatic processes, has a significant impact on hydrothermal activity beneath the TAG and potentially other hydrothermal fields.

Figure 3 shows how heat and magma are extracted near a buried active detachment fault beneath the TAG field. Based on micro-earthquake data, de Martin et al. (2007) developed a graphic model to explain the geometry and characteristics of the TAG detachment fault (Fig.3). In de Martin et al. (2007)'s model, the detachment fault is a dome-shaped normal fault, which is entirely curved and extends into the lithospheric mantle. The dipping angle of the fault is 70^{o} from 3 km to 7 km beneath the seafloor, and microscale earthquakes are detected within this interval. Gabbros are crystallized and accumulated within the footwall of the fault during extension. Since the seismic data indicate there is no magma chamber immediately beneath the seafloor surface in the hanging wall of the detachment fault, hydrothermal circulation must penetrate to a great depth (up to 7 km) to extract sufficient heat to explain the observed vent fields. The heat is gathered at the bottom of the fault and travels through the hanging wall to the shallower depths. The micro-scale earthquakes disappear at and above 3 km, suggesting shallow extension is accommodated aseismically. The change from seismic to aseismic slip is attributed to the change of the dipping angle of the detachment fault to ~20^{o}. (de Martin et al., 2007; Humphris et al., 2015a).

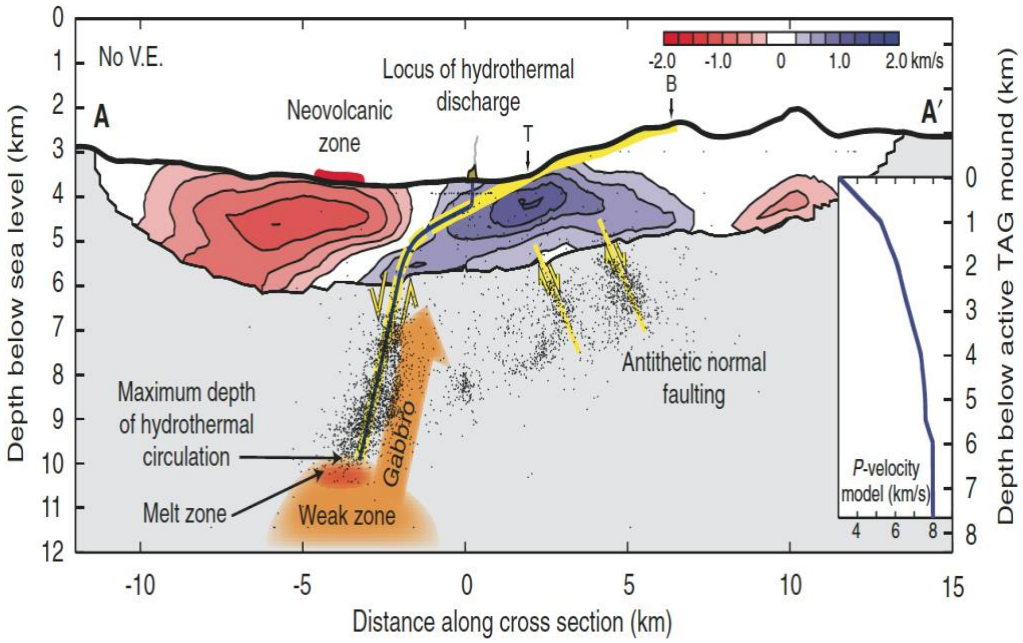

Figure 3. The cross-section of the detachment fault beneath the TAG field. Black dots are observed micro-earthquake hypocenters (de Martin et al., 2007).

Compared to asymmetrical accretion, Escartín et al. (2008) observed that symmetrical accretion is dominated by magmatic activity with high-angle faults buried and the generation of abyssal hills along symmetrical segments(Escartín et al., 2008). Seismic and hydrothermal activity (Fig.4) is lower due to decreased tectonic force. In this model, the reduced hydrothermal cooling elevates the top of the melting regime, which results in higher extents of melting and lower degrees of melt-rock interaction than asymmetrical segments, revealed by major element geochemistry in MORB (Escartín et al., 2008). The robust volcanic activity and relatively high magma flux beneath symmetrical segments lead to a smooth and inflated morphology at the seafloor (Murton and Rona, 2015).

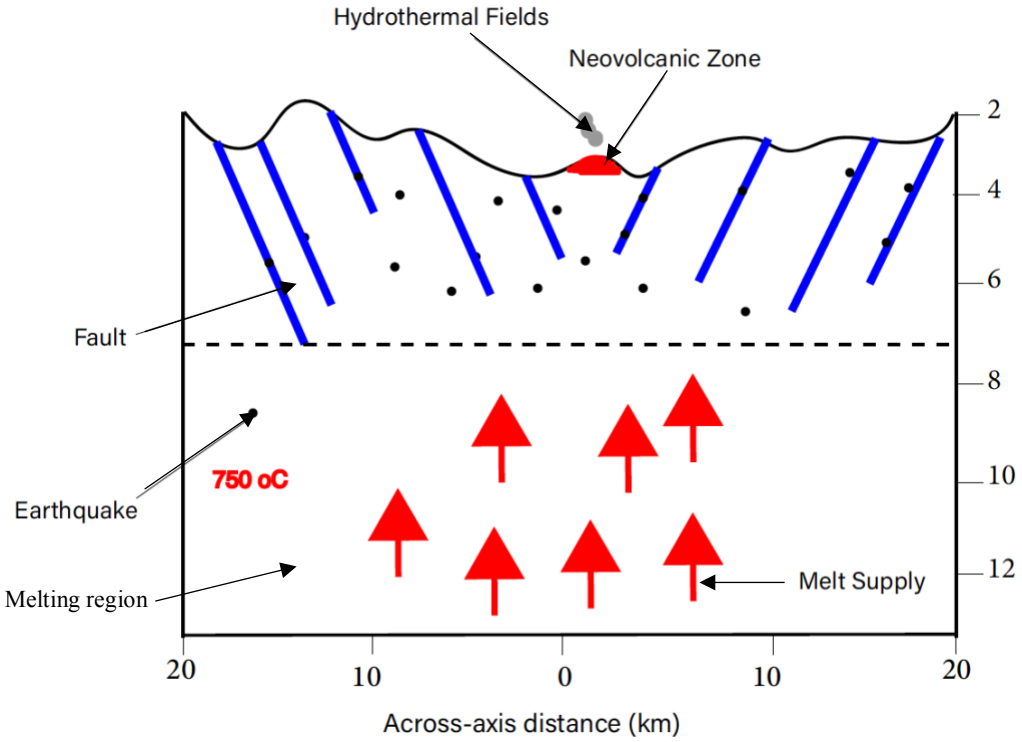

Figure 4. Cross section of a detachment fault-bearing ridge (after *Escartín et al., 2008*). In symmetrical segment systems, the top of the melting regime is high, which results in a high extent of melting and a thin lithosphere.

The discussions above and referenced studies suggest that the magnitude of magma supply may influence the formation of detachment faults, which is further a potential driving factor for determining whether a ridge segment is symmetrically or asymmetrically accreted. Relatively, Xu et al. (2009) argued that the gabbros exposed on the Kane OCC footwall and shape of Kane OCC are products of the dynamic changes in magma supply and mantle fertility, or decompression melting, specifically near the exhuming footwall of a detachment fault where lower crustal intrusion of plutons was enhanced. Since basalts are the products of magma eruption and cooling processes, the geochemistry of basalts from different segment styles will potentially imply what are the dominant factors for

driving the accretionary style at slow-spreading ridges, which in turn affects seafloor constructions at the MAR.

2.2 Factors for influencing MORB construction

This study aims to investigate the principal drivers of magma supply, and therefore of ridge construction style, using MORB geochemistry; effective interpretation of such data, however, requires a good understanding of the variables that control magma generation in the mid-ocean ridge settings.

2.2.1 The effect of mantle temperature

The major mechanism for generating MORB is partial melting of the lherzolitic mantle by decompression beneath mid-ocean ridge spreading centers (e.g., Lambart et al., 2009, and references therein). If the mantle is homogeneous, mantle temperature is the main control over variations in the melting regime. Klein and Langmuir (1987) suggested that the peridotite mantle at different regions starts to melt at various depths, depending on the source mantle's potential temperature (T_p). Variations in the initial melting pressure, extent of melting, total melting column length and resulting oceanic crustal thickness are thus all products of mantle temperature.

This scenario is summarized in Fig. 5, which shows two melting regimes. In both scenarios, the solid black lines indicate the solidus, below which the source mantle remains solid and above which are partially molten materials. In Fig. 5a, the mantle source has a

higher potential temperature (T_p). The hotter mantle intersects the solidus at a greater depth and starts to melt deeper during convective upwelling, which results in a higher initial melting pressure (P_i) and a longer melting interval. All these factors contribute to creating a larger mean and maximum extent of melting, and therefore a thicker crust with shallower seafloor depths (Klein and Langmuir, 1987; White and Klein, 2013). The mantle in Fig. 5b has a lower T_p and therefore intersects the solidus and starts to melt at a shallower depth. Consequently, this cooler mantle will result in a lower P_i and a shorter melting column, which leads to a smaller mean and maximum extent of melting and thus a thinner oceanic crust (Klein and Langmuir, 1987; White and Klein, 2013; Langmuir et al., 1992). Therefore, mantle temperature positively correlates with initial melting pressure and crustal thickness. Crustal thickness is also inversely related to seafloor depth at the ridge axis, such that mantle temperature is negatively correlated with axial depth (Klein and Langmuir, 1987; Bourdon et al., 1996; White and Klein, 2013; Niu Y., 1997, and references therein).

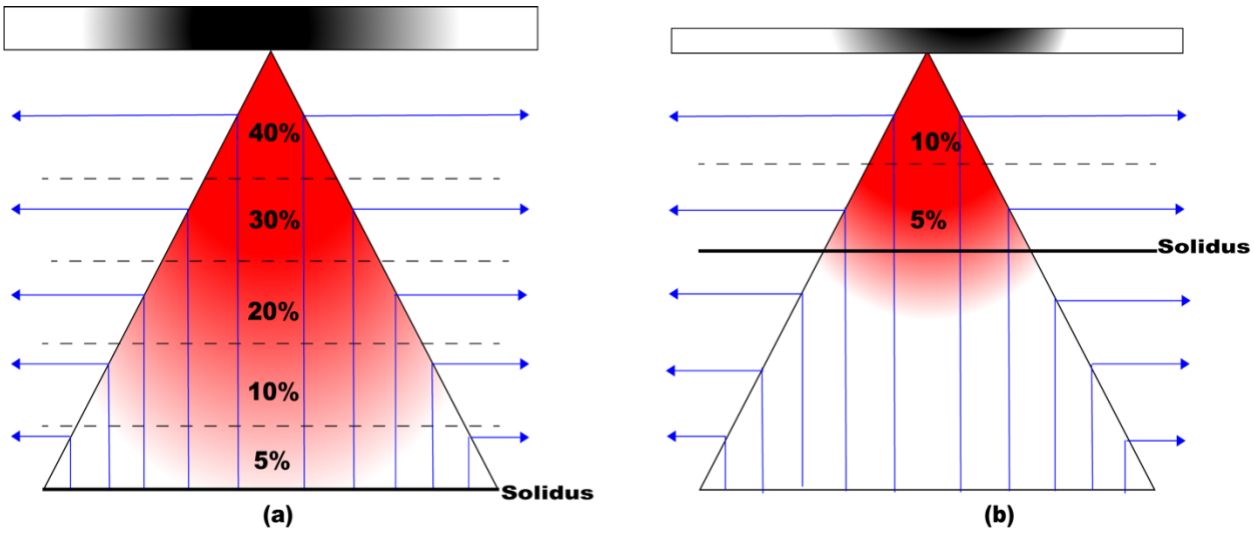

Figure 5. Steady-state passive upwelling and melting regime beneath mid-ocean ridges, after *White and*

Klein (2013). Blue curves with arrows indicate solid mantle convection paths through the melting regime; dashed lines indicate the extent of melting. Scenario (a) indicates the hotter mantle intersects the solidus at a deeper depth, which causes a larger mean and maximum extent of melting; scenario (b) shows the cooler mantle intersects the solidus at a shallower depth, which causes a smaller mean and maximum extent of melting.

The effects of changing extents of melting due to various T_p can be preserved in some major element concentrations.). Klein and Langmuir (1987) systematically summarized the general behaviors of MgO, FeO, Na_2O, Al_2O_3 and CaO during melting processes. MgO increases with increasing degree of melting (F) at a steady pressure, whereas FeO remains fairly constant with increasing F. Sodium behaves as a moderately incompatible element during partial melting, and Na_2O exhibits highest contents at the smallest F and decreases with an increasing F (Jaques and Green, 1980; Dick et al., 1984). Similar to Na_2O, Al_2O_3 has the highest concentration in melts when F is the smallest and decreases with an increasing F (Fujii and Scarfe, 1985). The behavior of CaO in the melting process depends strongly with the existence of clinopyroxene: CaO increases as clinopyroxene melts; when clinopyroxene no longer exists in the residual solid, CaO will decrease during the rest melting process (Klein and Langmuir, 1987). Therefore, the CaO/Al_2O_3 ratio may indicate when the clinopyroxene melts out during a melting process.

The scenario described above is based on two premises: first, the system is a passive upwelling and melting regime (i.e., upwelling is a passive convection response to divergence). In reality, the melting flow can be “active” (e.g., mantle plume-driven) or more complex (e.g., Scotti and Stevenson, 1989; Putirka et al., 2007). Second, that the

source mantle is homogeneous. However, in reality, there are several aspects of MORB composition cannot be simply explained by a homogeneous mantle source, such as variations in trace element abundance (e.g., Allegre et al., 1995; Stracke and Bourdon, 2009). Multiple lines of evidence also indicate that garnet-bearing pyroxenite plays an important role in generating MORB (e.g., Lambart et al., 2016; Hirschmann and Stolper, 1996). Therefore, we must also consider the role of mantle source heterogeneity on magma generation.

2.2.2 The effect of mantle source heterogeneity

2.2.2.1 The scale of mantle heterogeneity

Many studies of the major and trace element and radiogenic isotope compositions of MORB suggest that the underlying mantle source is heterogeneous on various length scales (e.g., Sims, Hart, et al., 2008; Prytulak and Elliott, 2009; Claude-Ivanaj et al., 2001; Lyubetskaya and Korenaga, 2007; Lambart et al., 2016; Hirschmann et al., 2003; Bourdon et al., 2005; Kogiso et al., 2004; Elkins et al., 2016; Koornneef et al., 2012; Hofmann, 2003). Based on observed geochemical variations in oceanic basalts, some authors have stated that mantle heterogeneity on a scale of 10^2-10^4 km is sufficiently large to explain the chemical variations in MORB (e.g., Hart et al., 1973; White and Schilling, 1978; Dupre and Allegre, 1983), whereas Zindler and Hart (1986) argued that for oceanic island basalts (OIB), the mantle is heterogeneous on a much smaller scale (less than 1 km) and must be

effectively homogeneous only on a 20-100 km scale to cause isotopic variations in basalts' final compositions. Kogiso et al. (2004), however, demonstrated that centimeter-sized heterogeneous parcels are large enough to produce distinct chemical compositions in basalts. Meibom and Anderson (2004) further suggested that the isotopic variations observed in MORB and OIB are the results of homogenization by partial melting and melt mixing on a heterogeneity scale of 10^{2}-10^{5} km in the upper mantle. More recent modeling studies, such as Liu and Liang (2017) suggested that the heterogeneity scale in the upper mantle should be km-sized to preserve variations in MORB. These length scales are relevant to MORB heterogeneities observed down to a small spatial scale (e.g., EPR) and at the second-order segment scale of tens of kilometers, if such heterogeneities are preserved in basalts.

2.2.2.2 Evidence for heterogeneity from major elements

Several major elements (such as Na, Ca, Al, Fe and Ti) exhibit distinct enrichments or depletions in basalts, attributed to specific lithological sources in the mantle. For example, Klein and Langmuir (1987) plotted regional average values of $Na_{8.0}$ (concentration of Na_2O corrected for fractional crystallization by olivine removal to an initial parent MgO concentration of 8 wt%). CaO/Al_2O_3 and $Fe_{8.0}$ (FeO content of MORB at 8% wt MgO) versus regional average axial depths demonstrate that major element

heterogeneity exists at regional scales (Fig. 6). In addition to mantle temperature-driven trends in all three plots, where $Na_{8.0}$, $Fe_{8.0}$ and CaO/Al_2O_3 concentrations of global MORB either positively or negatively correlate with axial depths, some areas show distinct local systematics that cannot be solely attributed to mantle temperature variations. In Fig. 6a, data from different ocean basins fall into distinct domains (circled areas). Samples from South Atlantic ridges and Indian Ocean ridges generally are more enriched in Na_2O (mean $Na_{8.0}$ = 2.67 wt. %) than samples from North Atlantic ridges (mean $Na_{8.0}$ = 2.27 wt. %), while samples from the East Pacific Rise have moderate Na_2O contents (mean $Na_{8.0}$ = 2.45 wt. %). The regional differences in Na_2O concentration are interpreted to reflect global major element heterogeneity in the source mantle, which might also be an indicator of lithological heterogeneity.

While Fig. 6a shows that major element contents in MORB are globally heterogeneous, Fig. 6b and 6c demonstrate that there are also variations in major element composition within a single region. In Fig. 6b, although small deviations are observed, Atlantic MORB with axial depths < 1000 km display a positive correlation between CaO/Al_2O_3 and axial depth (circled area). If the mantle source for generating the Atlantic MORB is homogeneous and this correlation was driven by mantle temperature and extent of melting, we should observe a similar trend for $Fe_{8.0}$ versus axial depth. Figure 6c, however, exhibits a convex trend from 0-1000 km depth (circled area). Clinopyroxene crystallization could cause FeO concentrations in magmas to increase and CaO/Al_2O_3 to

decrease, since clinopyroxenes have lower FeO than their host magmas (e.g., Dungan and Rhodes, 1978; Klein and Langmuir, 1987). The negative trend between CaO/Al_2O_3 and $Fe_{8.0}$ at 0-500 km axial depths can thus be explained by enhanced clinopyroxene crystallization beneath the ridges. However, clinopyroxene fractionation cannot explain the positive trend observed from 500-1000 km axial depth (Fig. 6c), suggesting major element heterogeneity is a better explanation. Lambart et al. (2009) noted that the behavior of FeO during partial melting is different for peridotite and pyroxenite sources, such that melts derived from most pyroxenites have higher FeO contents; one explanation for generating unusually high FeO concentrations in MORB between 0-500 km axial depth is thus the presence of pyroxenite rocks in the mantle source.

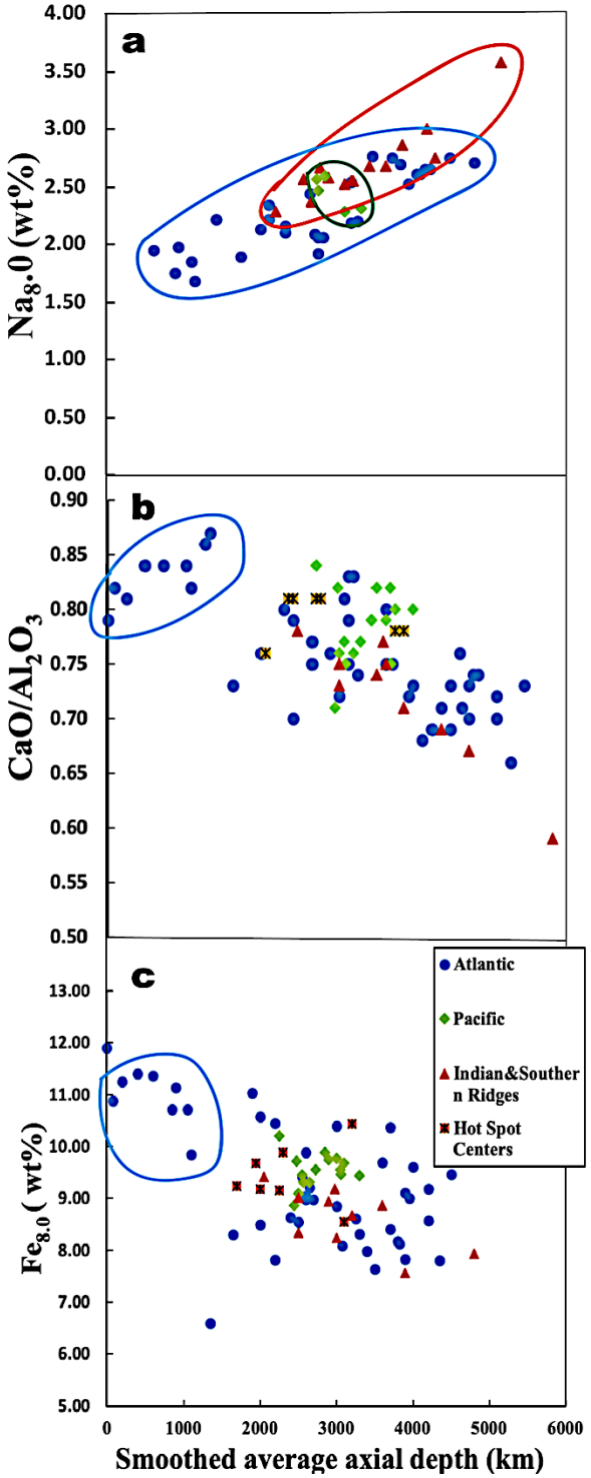

Figure 6. Major element compositions vs. smoothed axial depth for MORB, after *Klein and Langmuir (1987)*, for (a)$Na_{8.0}$, (b) CaO/Al_2O_3 and (c) $Fe_{8.0}$versus regional averaged axial depth for various types of MORB, including normal MORB (N-MORB) from the Atlantic, Pacific, and Indian Ocean ridges and enriched MORB (E-MORB) from hot spot centers (such as Iceland, the Azores, and the Galapagos, etc.,).

Besides Na_2O, CaO, Al_2O_3, and FeO, TiO_2 in MORB is also a possible indicator of source lithology. TiO_2 behaves as a moderately incompatible element during partial melting and partitions differently between each lithology (peridotite or pyroxenite) and co-existing melt (Langmuir et al., 1992; Lambart et al., 2009; Prytulak and Elliott, 2009). The TiO_2 contents in pyroxenites and peridotites are also significantly different: pyroxenites can hold up to 3% TiO_2, whereas fertile peridotites commonly have 0.1-0.3% TiO_2 (Lambart et al., 2009). Two minerals that exert a major control on Ti partitioning during partial melting processes are clinopyroxene and garnet (Prytulak and Elliott, 2007). Since peridotite and pyroxenite have different modes and stability pressure fields for garnet and clinopyroxene, the concentration of TiO_2 in basalt may reflect the contents of these two minerals in the source mantle. High TiO_2 in MORB may thus indicate that the predominant lherzolitic partial melts have been mixed with major element-enriched materials such as recycled mafic crust, or alternatively pelagic and continental subducted sediments (Prytulak and Elliott, 2007).

Alternatively, CaO/Al_2O_3 may be a product of melt-rock interaction processes, as such reactions cause enrichments in Al_2O_3 and MgO and depletions in CaO and SiO_2 (Lissenberg and Dick, 2008).

2.2.2.3 Evidence from trace elements

Mid-ocean ridge basalts derive from mantle reservoirs that have been significantly depleted by the extraction of the continental crust in Earth's early history, and then re-enriched by recycling of crust into the convecting mantle (Arevalo and McDonough, 2010; Hofmann, 1988). Studying trace elements is a critical way to examine mantle source heterogeneity, since (1) much like TiO_2, the melt partitioning behavior of trace elements in

peridotite and pyroxenite are different (e.g., Stracke and Bourdon, 2009; Langmuir et al., 1992), and (2) abundances of trace elements are different in recycled and residual mantle reservoirs (e.g., Niu and Batiza, 1997; Saunders et al., 1988).

Figure 7 shows partitioning behavior of both individual trace elements and their ratios in pyroxenite and peridotite partial melts. In Fig. 7a, highly incompatible elements (such as Ba, Th, U, Nb and La, which have partition coefficients $D << 1$) behave distinctively in pyroxenite and peridotites rocks during melting. These elements can thus be used as source heterogeneity indicators (Pertermann and Hirschmann, 2002). Barium and La are more incompatible in pyroxenite than peridotite, while Sr behaves in the opposite fashion. Elemental ratios involving Ba (such as Ba/Th) are thus potentially useful for evaluating the chemical differences in MORB compositions due to source heterogeneity (Stracke and Bourdon, 2009). Other trace element ratios such as Sm/Yb and Lu/Hf are sensitive to the presence of garnet in the residual mantle. Thus, these ratios can serve as parameters for testing the melting depth and the modes of garnet in both peridotite and pyroxenite, and to further examine the distributions of peridotite and pyroxenite in the source (Hirschmann and Stolper, 1996; Stracke and Bourdon, 2009).

Global MORB are generally divided into two groups based on trace elemental distributions: “normal-type” MORB (N-MORB) and “enriched-type” (E-MORB) (Schilling, 1973). N-MORB represent most MORB found globally and characterized by depletions in highly incompatible elements compared to other elements (e.g., Sun and

McDonough, 1989; Hofmann, 1988, 2003; Arevalo and McDonough, 2010 and references therein), which result in distinctive trace element ratios (e.g., La/Sm <1). On the contrary, E-MORB are more enriched in highly incompatible elements, which results in trace element ratios different from N-MORB (e.g., La/Sm >1, Arevalo and McDonough, 2010). Global MORB have an average Th/U ratio of 2.87 (Arevalo and McDonough, 2010), N-MORB generally have a mean Th/U lower than 2.87 (e.g., 2.5, Goldstein et al., 1989) and E-MORB have a higher mean Th/U (e.g., 2.94; Waters et al., 2011). Enrichments of trace elements may also be produced by events from either the deep mantle (e.g., prior to melting) or shallow depths (e.g., after partial melting starts) (Avrevalo and McDonough, 2010). Trace elements also show various distributions in different ocean basins: Atlantic MORB are enriched in highly incompatible elements (e.g., Sr, Hf, Th, U and Nb) and moderately incompatible elements (e.g., Er and Yb) compared to other MORB. The enrichment in both highly and moderately incompatible elements may due to small extents of melting or large degrees of fractional crystallization beneath the MAR (e.g., Niu and Hékinian, 1997). Pacific Ocean MORB, on the other hand, are generally depleted in highly incompatible elements (such as Ba, Th and U), which may due to high extents of melting beneath this fast-spreading ridge system (Arevalo and McDonough, 2010). Indian Ocean MORB are depleted in moderately incompatible elements and heavy REE, which may be attributed to melts from a distinct lithology (Arevalo and McDonough, 2010).

In addition to using trace elements to evaluate source heterogeneity, geochemists may

also select moderately incompatible trace elements such as Sr, Nd, Hf, Zr, Sm and Yb and their ratios to analyze MORB composition variations created by different extents of melting (i.e., T_p). The bulk D of these elements in pyroxenites are about 5 times higher than in peridotite (Fig. 7a, Stracke and Bourdon, 2009), so the contents of these elements in erupted lavas should vary if the mantle source is heterogeneous. If the bulk rock D ratios of these elements (such as Sm/Yb) between pyroxenites and peridotite (Fig. 7b) do not exhibit large differences, however, it may indicate that the heterogeneity is averaged or homogenized by various extents of melting.

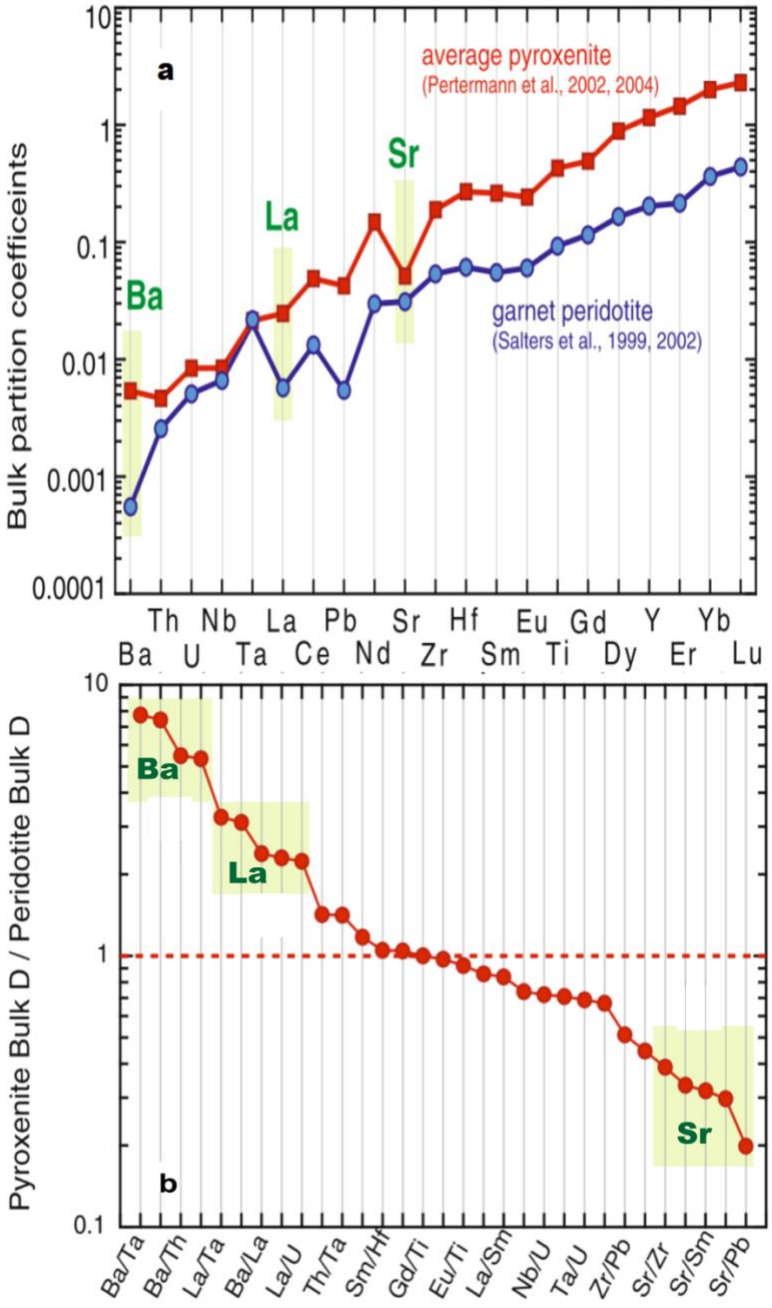

Figure 7. After *Stracke and Bourdon, (2009)*. (a) comparison of averaged bulk partition coefficients for pyroxenite and peridotite. (b) Comparison of averaged bulk partition coefficient ratios for pyroxenite and peridotite. The horizontal dashed line indicates that the bulk partition coefficient for pyroxenite equals to that for peridotite. Above the dashed line trace element ratios are more enriched in pyroxenite and below which trace element ratios are more enriched in peridotite.

2.2.3 The effects of melt-rock interactions in the lower oceanic crust

Besides events from the deeper mantle, near-surface processes also influence MORB geochemistry. Studies demonstrate that after partial melting, ascending segregated melts may react with surrounding cumulate minerals in the lower oceanic crust, which may change MORB compositions(Coogan et al., 2000; Kvassnes and Sweetman, 2004; Lissenberg and Dick, 2008).

Lissenberg and Dick (2008) have observed that CaO, Al_2O_3, MgO and SiO_2 in basalts are potentially affected by melt-rock interactions in the crust and systematically summarized possible effects of such reactions. CaO in melts likely decreases and MgO likely increases with increasing melt-rich interactions, due to olivine assimilation and simultaneous shallow clinopyroxene fractionation. Such interactions would likely also increase the Al_2O_3 contents in basaltic melts due to additional assimilation of Al-rich plagioclase cumulates, which is expected to occur in larger fractions than plagioclase removal. SiO_2 in melts may also decrease during complex melt-rock interactions, rather than increasing as predicted by simple crystal fractionation scenarios; this decreasing assimilated crustal assemblage has lower SiO_2 than the gabbroic assemblage fractionated from basaltic melts (Lissenberg and Dick, 2008).

3. Methodology

3.1 Sample preparation

Samples were collected from the Kane-Atlantis supersegment between 24°N and 30°N by dredging and gravity core during R/V Knorr expedition leg 207 in 2012. All basalt samples were hand-picked to select fresh, unaltered volcanic glass and remove all significant phenocrysts (e.g., plagioclase). After separating sufficient glass, separates were leached using a solution of 0.1 M oxalic acid with 2% H_2O_2 for 15 minutes in an ultrasonic bath and leached again using a solution of 0.1 M HCl and 2% H_2O_2 for an additional 15 minutes and rinsed three times in ultrapure water again. This leaching procedure was used to remove dust, palagonite, and surface deposits including MnO coatings(Elkins et al., 2016). Finally, the dried samples were hand-picked for a second time to verify that the glass was free of phenocrysts and visible surface alteration and coatings.

After the hand-picking and leaching procedures, all materials were dissolved using a series of strong acids (HNO_3, HCl, $HClO_4$, and HF) as follows. Each sample was weighed and transferred to a clean, pre-weighted 30 mL Savillex beaker. Then, concentrated HNO_3 and HF (2 mL concentrated HF per 500 mg sample material) were added to digest the samples. After the initial digestion, concentrated $HClO_4$ was added and the samples were fumed to dryness, after which they were immersed in a mixed solution of $HClO_4$, HCl, and ultrapure water, then fumed to dryness several more times. Samples were then redissolved in 3N HCl, transferred and centrifuged for 15 minutes, and the supernatant removed for

storage. Any remaining precipitate was returned to the beaker and again fumed using the HCl-$HClO_4$ mixture. This fuming and centrifugation process was iterated until all visible precipitates were fully dissolved. Samples were then diluted to a long-term stable concentration (8-10 mg rock/gram of solution) in 3N HCl and stored in clean, pre-weighed LDPE bottles for future analysis.

3.1.1 U and Th concentrations, $^{238}U/^{232}Th$

Dissolution was followed by an isotope dilution procedure. A precise amount of sample solution was transferred to a clean Savillex vial and weighed, aiming for an aliquot with approximately 5-10 ng U based on prior trace element measurements in the Kane-Atlantis region (e.g., Gale et al., 2013). The sample solution was then spiked by the addition of weighed quantities of known ^{233}U and ^{229}Th solutions, aiming for approximate target ratios of $^{233}U/^{238}U$ and $^{229}Th/^{232}Th$ of 1: 10 and 1 : 30, respectively. After spiking and digesting with $HClO_4$ on a hot plate for two days, 1 mL ultrapure water, 0.25 mL concentrated $HClO_4$ and 2 mL concentrated HNO_3 collectively were added to each sample. Solutions were fumed to dryness in this solution twice to ensure full spike-standard equilibration, and then the dried materials were wetted in HNO_3 and dried again to ensure conversion to nitrate form (Elkins et al., 2016; Sims, et al., 2008).

Uranium and Th were separated from the rock matrix using an anion column procedure in HNO_3 with methods after Sim et al (2008). The collected U and Th fractions

were dried and redissolved in 5% HNO_3 for mass spectrometry analysis.

The U and Th concentrations were measured by multi-collector inductively-coupled plasma mass spectrometry (MC-ICP-MS) using a Thermo Fisher NeptunePLUS instrument at the University of Wyoming. Uncertainties based on internal reproducibility are on the order of 0.1% for ($^{238}U/^{232}Th$) activity ratios (2σ), and the propagated uncertainties for mass bias corrections and external reproducibility are on the order of 0.3-0.6% for samples and 0.4% for standards. Mass bias was corrected using BHVO, W-1 and W-2 and acceptable ($^{238}U/^{232}Th$) value of 0.5% (Elkins et al., 2011).

4. Results

Table 2. Uranium and thorium isotope concentrations of the samples and standards analyzed in this study.

Sample Name	[Th][1] ug/g	[U] ug/g	Th/U	($^{238}U/^{232}Th$)[2]
Sample				
D01-6	0.14(8)	0.03(7)	3.96(8)	0.76(5)
D65-2	0.17(6)	0.06(1)	2.88(5)	1.05(1)
D2-SG	0.11(7)	0.04(5)	2.62(1)	1.15(8)
D58-3	0.13(5)	0.05(2)	2.56(9)	1.18(1)
D08-2	0.11(9)	0.04(5)	2.62(1)	1.15(8)
D13-SG	0.08(1)	0.03(1)	2.62(2)	1.15(8)
D10-2	0.07(5)	0.02(9)	2.59(5)	1.16(9)
D61-SG	0.14(2)	0.05(5)	2.59(9)	1.16(7)
D11-4	0.11(6)	0.04(8)	2.43(3)	1.24(7)
D09-SG	0.12(2)	0.03(5)	3.45(1)	0.87(9)
D12-SG	0.06(8)	0.04(3)	1.57(9)	1.92(1)
D16-SG	0.07(3)	0.03(2)	2.28(3)	1.32(9)
D14-SG	0.06(7)	0.02(7)	2.45(1)	1.23(8)
D17-SG	0.07(5)	0.02(7)	2.75(9)	1.09(9)
D15-SG	0.04(7)	0.02(5)	1.88(7)	1.60(8)
D22-2	0.09(3)	0.03(8)	2.35(5)	1.28(8)

Table 2 (continued)

Sample Name	[Th][1] ug/g	[U] ug/g	Th/U	(^{238}U/^{232}Th)[2]
D23-1	0.20(5)	0.07(1)	2.90(3)	1.04(5)
D26-2-SG	0.10(3)	0.02(5)	4.19(1)	0.72(4)
D32-5	0.10(1)	0.03(9)	2.59(3)	1.17(2)
D33-1	0.08(5)	0.03(7)	2.32(2)	1.30(6)
D32-SG	0.01(7)	0.006(3)	2.75(2)	1.10(3)
D50-5	0.12(6)	0.04(5)	2.79(2)	1.98(7)
D35-SG	0.13(5)	0.05(6)	2.43(4)	1.24(7)
D37-2	0.07(3)	0.01(8)	3.98(9)	0.76(4)
D42-2	0.179(6)	0.09(7)	1.84(6)	1.64(4)
D47-11	0.149(6)	0.05(7)	2.60(5)	1.16(5)
D48-3	0.12(5)	0.04(5)	2.77(5)	1.09(3)
D46-6	0.15(9)	0.06(7)	2.35(5)	1.28(8)
D42-SG	0.18(1)	0.07(1)	2.59(3)	1.17(1)
RC03	0.08(2)	0.03(4)	2.43(4)	1.24(7)
RC05	0.15(7)	0.06(2)	2.53(9)	1.19(5)
RC47	0.09(4)	0.03(5)	2.71(7)	1.11(7)
RC67	0.08(1)	0.03(6)	2.26(1)	1.34(2)
Standard				
BHVO-2	1.20(7)	0.41(6)	2.90(1)	1.04(6)
BHVO-3	1.09(7)	0.42(4)	2.58(8)	1.17(2)
W-1	1.90(5)	0.54(2)	3.47(1)	0.87(4)
W-1	1.05(9)	0.31(1)	3.41(3)	0.89(9)
W-2a	2.13(3)	0.50(3)	4.24(3)	0.71(5)

[1] Vales in parentheses indicate absolute 2σ standard error for the last digit expressed.

[2] Results are calculated using the following decay constants: $\lambda_{U\text{-}238} = 1.55 \times 10^{-10}$ a^{-1}(Jaffey et al., 1971), $\lambda_{Th\text{-}232} = 4.948 \times 10^{-11}$ a^{-1}(Le Roux, L.J., Glendenin, 1963).

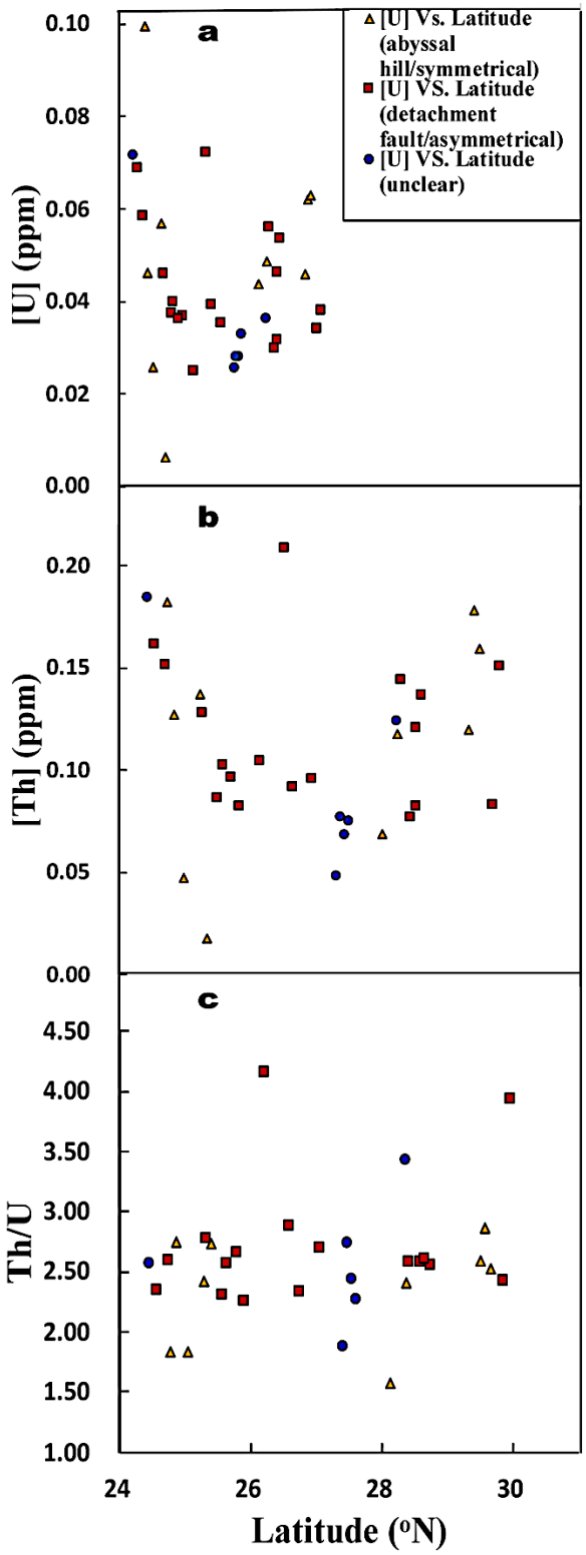

Figure 8. Plots of (a) uranium concentrations, (b) thorium concentrations and (c) Th/U ratios vs. latitude for all samples (symmetrical/AB, asymmetrical/DB and unknown/UK) measured in this study.

Figure 8 shows the [U], [Th] and Th/U results for our 34 basalt samples. In Fig. 8a and 8b, samples from AB segments (n = 10) have more scattered patterns in both [U] and [Th] than samples from DB segments (n = 18), while Th/U ratios show the opposite pattern (i.e., a smaller range in basalts from symmetrical and asymmetrical segments, Fig. 8c). Similar outcomes can be derived from a basic statistical analysis of the results. Basalts from asymmetrical segments exhibit slightly more limited uranium and thorium concentration ranges than those from symmetrical segments, despite the larger number of DB samples in our data set: [U] = 0.03-0.07 ppm and [Th] = 0.08-0.21 ppm for DB versus [U] = 0.006-0.10 ppm and [Th] = 0.02-0.18 ppm for AB. Also, basalts from symmetrical segments have higher mean [U] but lower mean [Th] values ([U] = 0.0498 ppm and [Th] = 0.1153 ppm) than those from asymmetrical segments ([U] = 0.0436 ppm and [Th] = 0.1165 ppm), though these differences are small. Samples from asymmetrical segments have a higher Th/U mean value (2.7081) than those from symmetrical segments (2.3494). While the number of samples used in this analysis is limited, similar and more statistically significant variations are exhibited by prior published trace element data for the same ridge (Gale et al., 2013), as explored further below.

5. Discussion

Table 3. Major element compositions of basalt samples from asymmetrical (DB) and symmetrical (AB) segments of the Kane-Atlantis supersegment.

	Mean		Range		Variance[3]		T Stat[2]	dF	P (2-tail)
	AB	DB	AB	DB	AB	DB			
MgO (wt%)	7.(9)	8.(2)[1]	6.4 - 10.4	5.3 - 10.6	0.4	0.4	5.7	527	1.60E-08
FeO (wt%)	9.(6)	9.(5)	7.6 -13.1	7.6 - 11.7	0.5	0.5	-1.3	495	0.2
Na_2O (wt%)	2.(9)	2.(8)	2.2 - 3.4	1.8 - 3.3	0.04	0.04	-2.7	524	0.007
CaO (wt%)	11.(3)	11.(3)	9.8 - 13.2	10.4 - 13.1	0.2	0.2	-1.6	474	0.1
Al_2O_3 (wt%)	15.(7)	15.(6)	14.0 - 19.4	9.6 - 13.3	0.6	0.3	-1.9	406	0.05
SiO_2 (wt%)	50.(4)	50.(8)	47.4 - 53.9	46.2 - 52.7	0.8	0.8	-0.9	522	0.4
TiO_2 (wt%)	1.(5)	1.(5)	0.9 - 1.4	0.9 - 2.1	0.05	0.05	0.4	505	0.6
CaO/Al_2O_3	0.7(2)	0.7(2)	0.62 - 0.85	0.65 - 0.83	0.002	0.001	0.1	389	0.9

[1] Numbers in parentheses indicate 2σ absolute standard deviations for the last digit expressed.

[2] Statistical analysis results of Welch's t-test. T Stat indicates the test statistic and measures the size of difference relative to the variation in the sample data; dF indicates degree of freedom; P indicate the 2-tails p-value .

[3] Variations of data from AB and DB segments in the unit of σ absolute standard deviation.›

Table 4. Trace element compositions of basalt samples from asymmetrical (DB) and symmetrical (AB) segments of the Kane-Atlantis supersegment.

	Mean		Range		Variance		T Stat[2]	dF	P (2-tail)
	AB	**DB**	**AB**	**DB**	**AB**	**DB**			
La (ppm)	2.(8)[1]	2.(8)	1.5 - 5.1	0.9 - 7.5	0.6	0.6	-0.2	233	0.8
Sm (ppm)	3.(2)	3.(1)	1.8 - 4.8	1.6 - 4.6	0.3	0.3	-0.7	234	0.5
Yb (ppm)	3.(2)	3.(1)	2.0 - 4.6	0.4 - 4.1	0.2	0.3	-1.3	275	0.2
Th (ppm)	0.1(3)	0.1(2)	0.05 - 0.38	0.02 - 0.56	0.003	0.003	-1.04	243	0.3
U (ppm)	0.0(5)	0.0(5)	0.02 - 0.17	0.02 - 0.17	0.001	0.001	-1.54	217	0.52
Lu (ppm)	0.4(9)	0.5(0)	0.30 -0.76	0.36 - 0.65	0.005	0.005	0.71	228	0.47
Hf (ppm)	2.(4)	2.(4)	1.3 - 3.4	1.2 - 3.6	0.2	0.2	0.5	299	0.6
Sr (ppm)	116	109	87 - 149	0.01 - 119	663	197	-2.9	261	0.001

Table 4 (continued).

	Mean		Range		Variance		T Stat	dF	P (2-tail)
	AB	**DB**	**AB**	**DB**	**AB**	**DB**			
Nd (ppm)	8	8	4 - 14	0.01 - 14	9	9	-1	275	0.2
Ba (ppm)	9	8	2 - 35	2 - 59	9	9	-0.9	237	0.3
La/Sm	0.(9)	0.(9)	0.6 - 1.3	0.5 - 1.7	0.9	0.9	0.5	235	0.6
Sm/Yb	0.9(9)	0.9(8)	0.58 - 1.35	0.70 - 1.21	0.01	0.005	-0.44	211	0.66
Th/U	2.(6)	2.(6)	0.9 - 4.0	0.4 - 3.9	0.3	0.2	0.6	236	0.5
Lu/Hf	0.2(1)	0.2(1)	0.14 - 0.29	0.15 - 0.31	0.0006	0.0005	0.51	230	0.61
Sr/Nd	13	12	8– 27	0.4 – 21	9	10	-2	256	0.01
Ba/Th	69	67	44 - 119	32 - 159	167	176	-0.9	237	0.4

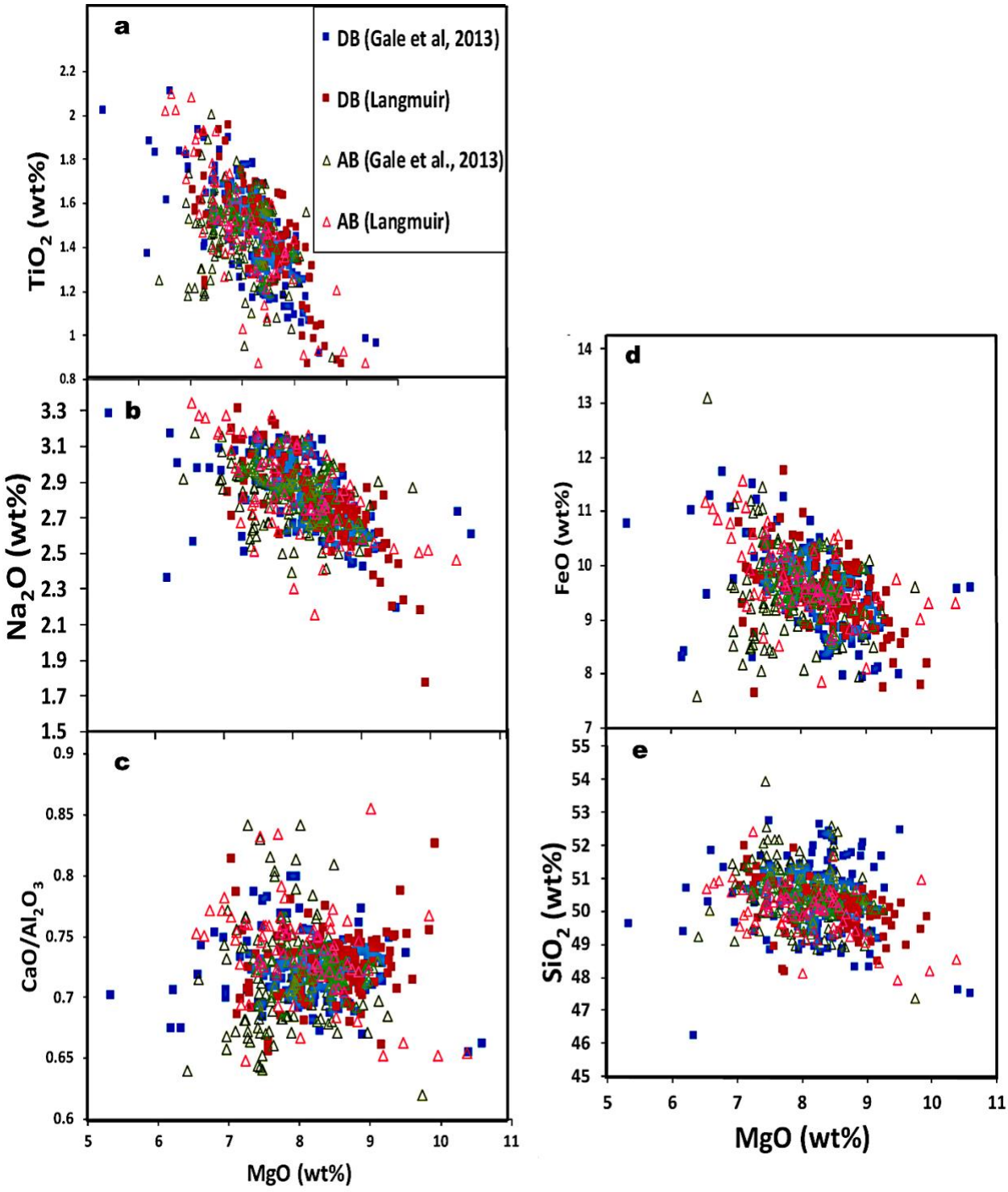

Figure 9. Plots of (a) TiO_2, (b) Na_2O, (c) CaO/Al_2O3, (d) FeO and (e) SiO_2 vs. MgO (wt%) for basalts from symmetrical (AB) and asymmetrical (DB) segments of the Kane-Atlantis supersegment (Gale et al., 2013, Langmuir, personal communication).

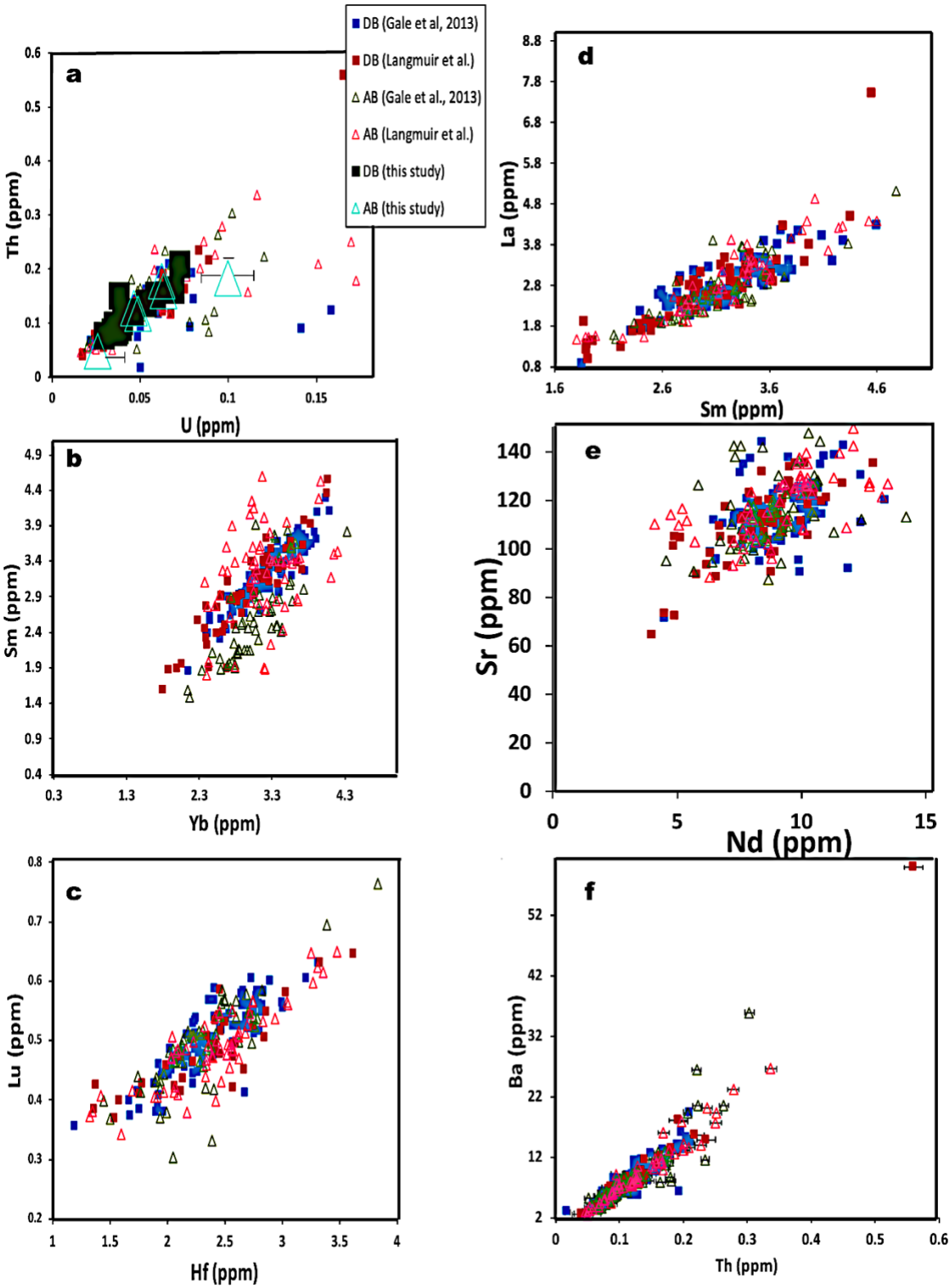

Figure 10. Diagrams showing trace element compositions in basalt samples from AB and DB segments: (a) Th vs. U, (b) Sm vs. Yb, (c) Lu vs. Hf, (d) La vs. Sm, (e) Sr vs. Nd, (f) Ba vs. Th (Gale et al., 2013, Langmuir, personal communication). In Fig. 11 (a) and x-axis in (f), 2σ standard errors are added to the DB and AB samples from this study.

One major goal of this study is to use coupled major and trace element data to explore the cause of observed variations in the compositions of basalts from the Kane-Atlantis supersegment. Compiling prior measured data from Gale et al. (2013) and Langmuir et al (personal communication) with the data measured in this study provides a more robust statistical analysis (n = 728).

Table 3 and 4 show results of statistical analyses for major element oxides (MgO, FeO, Na_2O, CaO, Al_2O_3, SiO_2, TiO_2), trace elements (La, Sm, Yb, Th, U, Lu, Hf, Sr, Nd, Ba) and trace element ratios (CaO/Al_2O_3, La/Sm, Sm/Yb, Th/U, Sr/Nd, Lu/Hf, Ba/Th). Statistical analyses show that samples from symmetrical (i.e., abyssal hill bearing or "AB"") and asymmetrical (i.e., detachment fault bearing or "DB") segments have equivalent compositions at the 95% confidence-level, expect for MgO, Na_2O, Sr and Sr/Nd contents. The p-values of these four data sets are lower than 0.05, which indicate that differences in mean MgO, Na_2O, [Sr] and Sr/Nd between samples from AB and DB segments are significantly large. Samples from DB segments also have a higher mean MgO content (8.2 wt%) and a slightly wider MgO range (5.3 – 10.6 wt%) than samples from AB segments (7.9 wt% and 6.4 – 10.4 wt%, respectively). The equivalent variances of MgO suggest the degrees of variations of MgO in samples from DB and AB segments are the same (Table 3). Samples from AB segments have a higher mean Na_2O content (2.9 wt%) and a wider Na_2O range (2.2 – 3.4 wt%) than samples from DB segments (2.8 wt% and 1.8 – 3.3 wt%, respectively). Again, the same variances in Na_2O suggest the equivalent compositions of

this oxide in samples from AB and DB segments (Table 3, Fig. 9). Samples from AB segments have a significantly higher mean [Sr] (116 ppm) but a narrower [Sr] range (87 – 149 ppm) than samples from DB segments (109 ppm and 0.01 – 119 ppm, respectively).

Processes that may cause the observed major and trace element variations may either derive from the convecting mantle, i.e., within the melting regime, or from shallower depths during lithospheric transport and emplacement. In the following discussion, three potential explanations are considered for the observed patterns: differences in the mean extent of melting due to mantle temperature variations beneath symmetrical and asymmetrical segments, mantle source heterogeneity, and assimilation and fractional crystallization (AFC) processes in the lithosphere.

5.1 Mean extents of melting beneath symmetrical and asymmetrical segments

Prior published literature (e.g., Klein and Langmuir, 1987; Escartín et al., 2001) has suggested that the mantle potential temperature (T_p) gradually decreases southward along the MAR from the Azores Islands, which in turn decreases the crustal thickness along the MAR from north to south. Decreasing T_p also slightly reduces the degree of mantle melting (F) toward the south, which elevates some major element concentrations (e.g., $Na_{8.0}$) in the residual basalt (e.g., Murton and Rona, 2015; Klein and Langmuir, 1987). Therefore, some variations in major element geochemistry may be the results of changing T_p and F. As mentioned above, asymmetrical segments are expected to overlie melting regimes with

lower mean extents of melting (hereafter referred to as "F") and lower melt supply than symmetrical segments, since the formation of detachment faults beneath asymmetrical segments may require low magmatic activity (e.g., Murton and Rona, 2015; Humphris et al., 2015). Assuming the source beneath the Kane-Atlantis supersegment is compositionally homogeneous peridotite and T_p is the only factor affecting MORB generation, one would expect lower mean concentrations of SiO_2 and CaO/Al_2O_3, and higher mean concentrations of Na_2O, FeO, TiO_2 and Al_2O_3 in samples from DB segments compared to samples from AB segments, if detachment faulting is indeed driven by low melt fractions in the mantle source (e.g., Klein and Langmuir, 1987; Paquet et al., 2016). However, statistical analyses show similar concentrations and distributions of these elements in samples from AB and DB segments (Table 3). This discrepancy either means the expectation of different melt fractions beneath AB and DB segments is incorrect, or the difference between F_{AB} and F_{DB} is small and the observed variations are controlled more strongly by a factor other than mantle temperature.

To test for the effects of T_p variations more quantitatively, I use a modal batch melting model to calculate average F_{AB} and F_{DB} values. The batch melting model and relevant equations are summarized in Appendix A. Since moderately incompatible elements (e.g., Sr, Hf, Sm) are sensitive to the change in melt fraction variations driven by T_p (Stracke and Bourdon, 2009), the mean concentrations of these elements in basalts from AB and DB segments may provide useful constraints on F_{AB} and F_{DB}. Table 5 shows parameters for

melting calculations performed here for the elements Sm, Yb, Lu, Hf and Nd. Estimated concentrations of these elements in the mantle source and mineral modes (57% olivine, 28% orthopyroxene, 13% clinopyroxene and 2% spinel) assuming a depleted mantle peridotite source after Workman and Hart (2005). The melt/mineral partition coefficients (D) for each element in every mineral are from Kelemen et al. (2004), and bulk D rock values for these elements are weighted averages of mineral/melt D values using mineral modes (e.g., Zou, 2010). Table 5 shows the results of F_{AB} and F_{DB}.

Table 5. Calculations of F_{AB} and F_{DB} using a modal batch melting model.

	C_o[1]	$D^{bulk,\ 2}$	C_{AB}[3]	F_{AB}	C_{DB}[4]	F_{DB}
Sm	0.239	0.044	3.165	0.033	3.114	0.034
Yb	0.365	0.097	3.218	0.018	3.138	0.021
Lu	0.058	0.107	0.491	0.012	0.497	0.011
Hf	0.157	0.046	2.364	0.022	2.391	0.021
Nd	0.581	0.027	8.572	0.042	8.932	0.039

[1] Estimated initial source concentrations from *Workman and Hart (2005)*.

[2] Bulk partition coefficient of each element, calculated from *Workman and Hart (2005)* and *Kelemen et al. (2004)*; and mineral modes of major minerals from from *Workman and Hart (2005)*.

[3, 4] Mean element concentrations in ppm of AB samples and DB samples, from Table 3.

The batch model calculations show that the ranges and the averages of F_{AB} (1.2 – 4.2%

and 2.6%, respectively) and F_{DB} (1.1 – 3.9% and 2.5%, respectively) are very similar, which is inconsistent with the expectation of a significant difference between segment styles (i.e., $F_{AB} > F_{DB}$). Both F_{AB} and F_{DB} are lower than typical batch melting calculations of melting along mid-ocean ridges (which has an F value ranging from 5%~10%), since we neglected the presence of garnet in the source. The calculated mean extents of melting beneath symmetrical and asymmetrical segments of the Kane-Atlantis supersegment are fairly constant, and extent of melting along thus likely does not control the observed compositions in the basalts. This interpretation further confirms that mantle temperature is not the dominant factor controlling segment style. This finding is consistent with the morphologic variations along the Kane-Atlantis ridges, which indicate a slight increase in crustal thickness southward but no preferential distribution of detachment-faulted segments with latitude. Below we consider two alternatives likely to be more significant on segment length scales, small scale mantle heterogeneities and melt-rock interactions in the lithosphere.

5.2 Mantle source heterogeneity beneath symmetrical and asymmetrical segments

The higher Na_2O and Sr contents in samples from AB segments compared to samples from DB segments may imply that symmetrical segments overlie a more fertile mantle peridotite source, which is consistent with the lower MgO content in AB segments samples.

However, since Al_2O_3 and FeO behave similarly to Na_2O during melting (Klein and Langmuir, 1987), the contents of these oxides should also be higher in AB segment samples than DB segment samples, which is not observed in Table 3. Compared to the significant difference of the mean Sr concentrations between samples from AB and DB segments, the enrichments of major elements in the source mantle are not as obvious as trace elements.

Additionally, the elemental variations between samples from AB and DB segments may be caused by lithologic heterogeneity. Table 3 reports a lower mean MgO content in samples from AB segments than DB segments, and Fig. 9 shows that most AB segment data span a moderate MgO range (6 – 10 wt%) and DB segment data cover a slightly higher range (5 – 11 wt%). The lower mean MgO content in AB segment samples compared to DB segment samples may due to a higher proportion of pyroxenites in the melting mantle region (Lambart et al., 2009). Table 4 and Fig. 10e show that differences in [Sr] and Sr/Nd between samples from AB and DB segments are statistically significant and AB segment samples have higher [Sr] and Sr/Nd compared to DB segment samples. Salters and Stracke (2004) suggested that a pure peridotite mantle source is expected to produce low Sr/Nd ratios because Sr and Nd are barely fractionated during typical peridotite melting. Since Sr is more compatible than Nd in pyroxenites (Stracke and Bourdon, 2009), on the other hand, pyroxenite melting produces notably higher Sr/Nd ratios in basalts: a pure peridotite melting produces a Sr/Nd content ranging from 10 – 15, whereas a mixed peridotite-pyroxenite source would yield a Sr/Nd content ranging from 15 – 35 at the same mantle

potential temperature (Stracke and Bourdon, 2009). Therefore, one explanation for these elemental distribution differences is that the mantle source beneath symmetrical segments may contain a higher proportion of pyroxenites compared to the source beneath asymmetrical segments.

5.3 Assimilation and fractional crystallization (AFC) beneath symmetrical and asymmetrical segments

An alternative explanation for the different distributions of MgO and Na_2O in samples from AB and DB segments is that the basalts have been affected by crustal assimilation and melt-rock interactions in the lithosphere to different degrees beneath symmetrical and asymmetrical segments.

Fractional crystallization may play an important role in affecting MORB compositions (e.g., Lissenberg and Dick, 2008; Depaolo, 1981; Langmuir, 1989; Standish et al., 2008; Arevalo and McDonough, 2010; Kuritani et al., 2005), and may occur at both low ($P < 4$ kbar) and high ($P > 8$ kbar) pressures (Lissenberg and Dick, 2008; Patiño Douce, 1997). Fractionation at low pressure may also generate magmas with different compositions from those that evolve at high pressures: in low-pressure crystal fractionation, olivine and plagioclase fractionate from ascending melts first, followed by clinopyroxene. At high pressures, clinopyroxene fractionation dominates over olivine and plagioclase removal because the clinopyroxene stability field extends at the expense of plagioclase and

olivine with increasing pressure (e.g., Grove et al., 1992; Presnall et al., 1978; Lissenberg and Dick, 2008).

The fractionation of clinopyroxene at high pressures increases the content of Na_2O in basaltic liquids because the fractionating clinopyroxene has a lower Na_2O concentration than its parental magmas (Klein and Langmuir, 1987; Paquet et al., 2016). The higher mean concentration of Na_2O in samples from AB segments may indicate a higher abundance of clinopyroxene fractionated beneath symmetrical segments than asymmetrical segments at high pressures. However, high -pressure crystallization would fractionate clinopyroxene with lower MgO concentrations, simultaneously causing MgO in the parental magma to increase. If such high-pressure fractionation was occurring beneath symmetrical segments, the basalts from these segments would have high MgO contents, but the opposite is observed here (Fig. 9, Table 3). Therefore, although high-pressure clinopyroxene fractionation may occur beneath symmetrical segments, it cannot explain the observed differences in MgO and Na_2O contents between samples from AB and DB segments.

A better explanation would be olivine, plagioclase and clinopyroxene fractionations at lower pressures beneath symmetrical segments. Fractionation of olivine would lower the MgO content in the melts, since fractionating olivine has a higher MgO concentration than its parental magmas (Lissenberg and Dick, 2008). A higher degree of olivine fractionation beneath symmetrical segments may first reduce the MgO content in the residual basalts, compared to samples from DB segments; then subsequent clinopyroxene fractionation

further elevates the Na_2O concentrations in samples from AB segments. This scenario would suggest that symmetrical segments experience higher degrees of low-pressure crystal fractionation than asymmetrical segments, consistent with shallower magma emplacement that observed in gabbros from OCCs (e.g., Wanless and Shaw, 2012).

Besides fractional crystallization, assimilation of surrounding wall rocks into ascending melts may also affect MORB compositions. Magma experiencing fractional crystallization may simultaneously assimilate surrounding rocks and react with pre-existing crustal cumulate minerals, since such crystallization releases heat that can melt neighboring rocks (Kuritani et al., 2005; Coogan et al., 2000; Kvassnes and Sweetman, 2004; Lissenberg and Dick, 2008). During melt-rock interactions, cumulate olivine, plagioclase and clinopyroxene may thus assimilate into ascending melts, and assimilation ratios of these minerals may in turn modify MORB compositions (Kuritani et al., 2005).

MgO contents in basalts are mainly affected by the assimilation ratio of plagioclase/olivine during melt-rock interactions. Plagioclase (which is Mg-free) dissolves faster than olivine (which contains Mg) in basaltic melts (Lissenberg and Dick, 2008). Therefore, a higher degree of melt-rock interactions may produce a larger plagioclase/olivine assimilation ratio and decrease MgO concentrations in residual basalts (Lissenberg and Dick, 2008). Compared to asymmetrical segments, a higher degree of fractional crystallization at low pressures beneath symmetrical segments as suggested above may concurrently trigger a higher degree of assimilation and melt-rock interactions

and yield a higher plagioclase/olivine assimilation ratio from surrounding rocks into basaltic melts. Although olivine assimilation would increase the MgO concentration in melts, the amount of fractioned olivine may exceed the assimilated olivine, such that the MgO content in samples from AB segments is still lower than that in samples from DB segments. In addition to major element concentrations, the overall higher [Sr] in samples from AB segments (Table 3, Fig. 10e) may suggest a higher degree of assimilation beneath symmetrical segments than asymmetrical segments, since Sr is more compatible in arising melts than surrounding rocks (e.g., Bohrson and Spera, 2003), a strong assimilation process would enhance the enrichment signal of [Sr] in basaltic melts. However, this interpretation is opposite to prior studies which suggested that asymmetrical segments host high degrees of melt-rock interactions and fractional crystallization in the lower crust, due to the presence of detachment faults beneath these segments (e.g., Escartín et al., 2008). Our study may indicate that detachment faults do not necessarily result in high melt-rock interactions, or that such effects are less important than mantle source heterogeneity effects on MORB compositions.

To sum up, the lower mean MgO and higher mean Na_2O and [Sr] in samples from AB segments may indicate that (1) the source mantle beneath symmetrical segments has a higher proportion of pyroxenites and/or a more trace element enriched peridotite than asymmetrical segments; (2) degrees of fractional crystallization and assimilation beneath symmetrical segments are higher than those beneath asymmetrical segments. This study

suggests that mantle source heterogeneity is more important than mantle temperature, fractional crystallization and assimilation in affecting ridge morphology along the Kane-Atlantis supersegment. Contrary to previous studies (e.g., Lissenberg and Dick, 2008), our study indicates that the magnitude of magma supply controls the formation of detachment faults beneath ridge segments. The slightly higher proportion of pyroxenites in the mantle source beneath symmetrical segments produces a slightly larger magma supply, which consequently prevents the formation of detachment faults beneath symmetrical segments. As a result of higher magma supply and lacking of detachment faults beneath symmetrical segments, the crust sufficiently accommodates seafloor spreading by classic symmetrical accretion. On the contrary, the lower proportion of pyroxenites in the source mantle beneath asymmetrical segments produces a slightly smaller magma supply, which promotes the formation of detachment faults beneath these segments. The lower magma supply and the presence of detachment faults cause the crust to insufficiently accommodate seafloor spreading by classic asymmetrical accretion. Additionally, the presence of detachment faults reduces degrees of melt-rock interactions and low-pressure fractional crystallization beneath asymmetrical segments.

6. Conclusion

Based on the combined major and trace element statistical analyses of basalt samples from symmetrical and asymmetrical segments, this study indicates that:

(1) Mantle source heterogeneity may be the dominant factor deriving differences in magma supply and the formation of detachment faults beneath asymmetrical segments along the Kane-Atlantis supersegment.

(2) Contrary to asymmetrical segments, the slightly higher magma supply beneath symmetrical segments is caused by a higher proportion of pyroxenites in the source mantle and/or a more trace element enriched peridotite.

(3) The higher magma supply beneath symmetrical segments prevents the detachment fault formation beneath these segments.

(4) The missing detachment faults and higher magma supply beneath symmetrical segments in turn increase degrees of assimilation and low-pressure fractional crystallization at shallow levels.

7. References

Abelson, M., and Agnon, A., 1997, Mechanics of oblique spreading and ridge segmentation: Earth and Planetary Science Letters, v. 148, p. 405–421, doi: https://doi.org/10.1016/S0012-821X(97)00054-X.

Allegre, C.J., Schiano, P., and Lewin, E., 1995, Differences between oceanic basalts by multitrace element ratio topology: Earth and Planetary Science Letters, v. 129, p. 1–12.

Arevalo, R., and McDonough, W.F., 2010, Chemical variations and regional diversity observed in MORB: Chemical Geology, v. 271, p. 70–85, doi: 10.1016/j.chemgeo.2009.12.013.

ASIMOW, P.D., 2001, Calculation of Peridotite Partial Melting from Thermodynamic Models of Minerals and Melts, IV. Adiabatic Decompression and the Composition and Mean Properties of Mid-ocean Ridge Basalts: v. 42, 963–998 p., doi: 10.1093/petrology/42.5.963.

Backer, E.., 2009, Relationships between hydrothermal activity and axial magma chamber distribution, depth, and melt content: Geochemistry, Geophysics, Geosystems, v. 10, doi: https://doi.org/10.1029/2009GC002424.

Blundy, J., and Wood, B., 2003, Partitioning of trace elements between crystals and melts: Earth and Planetary Science Letters, v. 210, p. 383–397, doi: 10.1016/S0012-821X(03)00129-8.

Bohrson, W.A., and Spera, F.J., 2003, Energy-constrained open-system magmatic processes IV: Geochemical, thermal and mass consequences of energyconstrained recharge, assimilation and fractional crystallization (EC-RAFC): Geochemistry, Geophysics, Geosystems, v. 4, doi: 10.1029/2002GC000316.

Boschi, C., Früh-Green, G.L., Delacour, A., Karson, J.A., and Kelley, D.S., 2006, Mass transfer and fluid flow during detachment faulting and development of an oceanic

core complex, Atlantis Massif (MAR 30°N): Geochemistry, Geophysics, Geosystems, v. 7, doi: 10.1029/2005GC001074.

Bourdon, B., Turner, S., Henderson, G.M., and Lundstrom, C.C., 2003, Introduction to U-series Geochemistry: Reviews in Mineralogy and Geochemistry, v. 52, p. 1–21, doi: 10.2113/0520001.

Bourdon, B., Turner, S.P., and Ribe, N.M., 2005, Partial melting and upwelling rates beneath the Azores from a U-series isotope perspective: Earth and Planetary Science Letters, v. 239, p. 42–56, doi: 10.1016/j.epsl.2005.08.008.

Bourdon, B., Zindler, A., Elliott, T., and Langmuir, C.H., 1996, Constraints on mantle melting at mid-ocean ridges from global 238U–230Th disequilibrium data: Nature, v. 384, p. 231–235, doi: 10.1038/384231a0.

Canales, J.P., 2010, Small-scale structure of the Kane oceanic core complex, Mid-Atlantic Ridge 23??30???N, from waveform tomography of multichannel seismic data: Geophysical Research Letters, v. 37, p. 1–6, doi: 10.1029/2010GL044412.

Canales, J.P., Sohn, R.A., and DeMartin, B.J., 2007a, Crustal structure of the Trans-Atlantic Geotraverse (TAG) segment (Mid-Atlantic Ridge, 26°10′N): Implications for the nature of hydrothermal circulation and detachment faulting at slow spreading ridges: Geochemistry, Geophysics, Geosystems, v. 8, doi: 10.1029/2007GC001629.

Canales, J.P., Sohn, R.A., and DeMartin, B.J., 2007b, Crustal structure of the Trans-Atlantic Geotraverse (TAG) segment (Mid-Atlantic Ridge, 26°10′N): Implications for the nature of hydrothermal circulation and detachment faulting at slow spreading ridges: Geochemistry, Geophysics, Geosystems, v. 8, doi: 10.1029/2007GC001629.

Cherkashov, G., Bel'tenev, V., Ivanov, V., Lazareva, L., Samovarov, M., Shilov, V., Stepanova, T., Glasby, G.P., and Kuznetsov, V., 2008, Two New Hydrothermal Fields at the Mid-Atlantic Ridge: Marine Georesources & Geotechnology, v. 26, p. 308–316, doi: 10.1080/10641190802400708.

Claude-Ivanaj, C., Joron, J.L., and Allègre, C.J., 2001, 238U230Th226Ra fractionation in

historical lavas from the Azores: Long-lived source heterogeneity vs. metasomatism fingerprints: Chemical Geology, v. 176, p. 295–310, doi: 10.1016/S0009-2541(00)00406-X.

Coogan, L.A., Kempton, Pamela, D., Saunders, A.D., and Norry, M.J., 2000, Melt aggregation within the crust beneath the Mid-Atlantic Ridge; evidence from plagioclase and clinopyroxene major and trace element compositions: Earth and Planetary Science Letters, v. 176, p. 245–257.

Depaolo, D.J., 1981, Trace element and isotopic effects of combined wallrock assimilation and fractional crystallization: Earth and Planetary Science Letters, v. 53, p. 189–202, doi: https://doi.org/10.1016/0012-821X(81)90153-9.

Dick, H.J.B., Fisher, R.L., and Bryan, W.B., 1984, Mineralogic variability of the uppermost mantle along mid-ocean ridges: Earth and Planetary Science Letters, v. 69, p. 88–106, doi: 10.1016/0012-821X(84)90076-1.

Dick, H.J.B., and Zhou, H., 2014, Ocean rises are products of variable mantle composition, temperature and focused melting: Nature Geoscience, v. 8, p. 68, https://doi.org/10.1038/ngeo2318.

Dungan, M., and Rhodes, J., 1978a, Residual glasses and melt inclusions in basalts from DSDP Legs 45 and 46: Evidence for magma mixing: Contributions to Mineralogy and Petrology, v. 67, p. 417–431, doi: 10.1007/BF00383301.

Dungan, M.A., and Rhodes, J.M., 1978b, Residual glasses and melt inclusions in basalts from DSDP Legs 45 and 46: Evidence for magma mixing: Contributions to Mineralogy and Petrology, doi: 10.1007/BF00383301.

Dupre, B., and Allegre, C.J., 1983, Pb-Sr isotope variations in Indian Ocean basalts and mixing interpretation: Nature, v. 303, p. 142–146.

Dupré, B., and Allègre, C.J., 1983, Pb-Sr isotope variation in Indian Ocean Basalts and mixing phenomena: Nature, doi: 10.1038/303142a0.

Elkins, L.J., Scott, S.R., Sims, K.W.W., Rivers, E.R., Devey, C.W., Reagan, M.K.,

Hamelin, C., and Pedersen, R.B., 2016, Exploring the role of mantle eclogite at mid-ocean ridges and hotspots: U-series constraints on Jan Mayen Island and the Kolbeinsey Ridge: Chemical Geology, v. 444, p. 128–140, doi: 10.1016/j.chemgeo.2016.09.035.

Elkins, L.J., Sims, K.W.W., Prytulak, J., Blichert-Toft, J., Elliott, T., Blusztajn, J., Fretzdorff, S., Reagan, M., Haase, K., Humphris, S., and Schilling, J.G., 2014, Melt generation beneath Arctic Ridges: Implications from U decay series disequilibria in the Mohns, Knipovich, and Gakkel Ridges: Elsevier Ltd, v. 127, 140–170 p., doi: 10.1016/j.gca.2013.11.031.

Elkins, L.J., Sims, K.W.W., Prytulak, J., Elliott, T., Mattielli, N., Blichert-Toft, J., Blusztajn, J., Dunbar, N., Devey, C., Mertz, D.F., Schilling, J.G., and Murrell, M., 2011, Understanding melt generation beneath the slow-spreading Kolbeinsey Ridge using238U,230Th, and231Pa excesses: Geochimica et Cosmochimica Acta, v. 75, p. 6300–6329, doi: 10.1016/j.gca.2011.08.020.

Escartín, J., Cannat, M., Pouliquen, G., Rabain, A., and Lin, J., 2001, Crustal thickness of V-shaped ridges south of the Azores: Interaction of the Mid-Atlantic Ridge (36°-39°N) and the Azores hot spot: Journal of Geophysical Research: Solid Earth, v. 106, p. 21719–21735, doi: 10.1029/2001jb000224.

Escartín, J., Smith, D.K., Cann, J., Schouten, H., Langmuir, C.H., and Escrig, S., 2008, Central role of detachment faults in accretion of slow-spreading oceanic lithosphere: Nature, v. 455, p. 790–794, doi: 10.1038/nature07333.

Fujii, T., and Scarfe, C.., 1985, Composition of liquids coexisting with spinel lherzolite at 10 kbar and the genesis of MORBs: Contributions to Mineralogy and Petrology, v. 90, p. 18–28, doi: https://doi.org/10.1007/BF00373037.

Gale, A., Dalton, C.A., Langmuir, C.H., Su, Y., and Schilling, J.G., 2013, The mean composition of ocean ridge basalts: Geochemistry, Geophysics, Geosystems, v. 14, p. 489–518, doi: 10.1029/2012GC004334.

German, C.R., Klinkhammer, G.., and Rudnicki, M.D., 1996, The Rainbow Hydrothermal Plume, 36°15′N, MAR: Geophysical Research Letters, v. 23, p. 2979–2982, doi: https://doi.org/10.1029/96GL02883.

Grove, T.L., Kinzler, R.J., and Bryan, W.B., 1992, Fractionation of Mid-Ocean Ridge Basalt (MORB) (J. P. Morgan, D. K. Blackman, & J. M. Sinton, Eds.): American Geophysical Union, 281–310 p., doi: 10.1029/GM071.

Haase, K., 2002, Geochemical constraints on magma sources and mixing processes in Easter Microplate MORB (SE Pacific): a case study of plume–ridge interaction: Chemical Geology, v. 182, p. 335–355, doi: https://doi.org/10.1016/S0009-2541(01)00327-8.

Hart, S.R., Schilling, J.-G., and POWELL, J.L., 1973, Basalts from Iceland and Along the Reykjanes Ridge: Sr Isotope Geochemistry: Nature, v. 246, p. 104–107, doi: 10.1038/physci246104a0.

Hirschmann, M.M., Kogiso, T., Baker, M.B., and Stolper, E.M., 2003, Alkalic magmas generated by partial melting of garnet pyroxenite: Geology, v. 31, p. 481–484, doi: 10.1130/0091-7613(2003)031<0481:AMGBPM>2.0.CO;2.

Hirschmann, M.., and Stolper, E., 1996, A possible role for garnet pyroxenite in the origin of the “garnet signature” in MORB: Contributions to Mineralogy and Petrology, v. 124, p. 185–208, doi: https://doi.org/10.1007/s004100050.

Hofmann, A.W., 1988, Chemical differentiation of the Earth: the relationship between mantle, continental crust, and oceanic crust: Earth and Planetary Science Letters, v. 90, p. 297–314, doi: 10.1016/0012-821X(88)90132-X.

Hofmann, A.W., 1997, Mantle geochemistry: the message from oceanic volcanism: Nature, v. 385, p. 219–229.

Hofmann, A.W., 2014, Sampling Mantle Heterogeneity through Oceanic Basalts: Isotopes and Trace Elements: Treatise on Geochemistry, v. 2, p. 61–101, doi: 10.1016/b978-0-08-095975-7.00203-5.

Hofmann, A., 2003, Sampling Mantle Heterogeneity through Oceanic Basalts: Isotopes and Trace Elements, *in* Treatise on geochemistry, v.2, p. 1-44, doi: 10.1016/B0-08-043751-6/02123-X

Howell, S.M., Olive, J.A., Ito, G., Behn, M.D., Escartín, J., and Kaus, B., 2019, Seafloor expression of oceanic detachment faulting reflects gradients in mid-ocean ridge magma supply: Earth and Planetary Science Letters, v. 516, p. 176–189, doi: https://doi.org/10.1016/j.epsl.2019.04.001.

Humphris, E., 2000, Constraints on the energy and chemical balances of the modern TAG and ancient Cyprus seafloor sulfide deposits: Journal of geo, v. 105, p. 28477–28488.

Humphris, S.E., Tivey, M.K., and Tivey, M.A., 2015a, Deep-Sea Research II The Trans-Atlantic Geotraverse hydrothermal fi eld : A hydrothermal system on an active detachment fault: Deep-Sea Research Part II, v. 121, p. 8–16, doi: 10.1016/j.dsr2.2015.02.015.

Humphris, S.E., Tivey, M.K., and Tivey, M.A., 2015b, The Trans-Atlantic Geotraverse hydrothermal field: A hydrothermal system on an active detachment fault: Deep-Sea Research Part II: Topical Studies in Oceanography, v. 121, p. 8–16, doi: 10.1016/j.dsr2.2015.02.015.

Ildefonse, B., Blackman, D.K., John, B.E., Ohara, Y., Miller, D.J., MacLeod, C.J., Abe, N., Abratis, M., Andal, E.S., Andréani, M., Awaji, S., Beard, J.S., Brunelli, D., Charney, A.B., et al., 2007, Oceanic core complexes and crustal accretion at slow-speading ridges: Geology, v. 35, p. 623–626, doi: 10.1130/G23531A.1.

Ito, G., and Mahoney, J.J., 2005, Flow and melting of a heterogeneous mantle: 1. Method and importance to the geochemistry of ocean island and mid-ocean ridge basalts: Earth and Planetary Science Letters, v. 230, p. 29–46, doi: 10.1016/j.epsl.2004.10.035.

J. Goldstein, S., Murrell, M.T., and Janecky, D.R., 1989, Th and U isotopic systematics of basalts from the Juan de Fuca and Gorda Ridges by mass spectrometry: Earth and

Planetary Science Letters, v. 96, p. 134–146, doi: https://doi.org/10.1016/0012-821X(89)90128-3.

Jaffey, A.H., Flynn, K.F., Glendenin, L.E., Bentley, W.C., and Essling, A.M., 1971, Precision measurement of half-lives and specific activities of U235 and U238: Physical Review C, v. 4, p. 1889–1906, doi: 10.1103/PhysRevC.4.1889.

Jaques, A.., and Green, D.., 1980, Anhydrous melting of peridotite at 0–15 Kb pressure and the genesis of tholeiitic basalts: Contributions to Mineralogy and Petrology, v. 73, p. 287–310, doi: https://doi.org/10.1007/BF00381447.

Jin, S., and Zhu, W., 2003, Present-day spreading motion of the mid-Atlantic ridge: Chinese Science Bulletin, v. 47, p. 1551, doi: 10.1360/02tb9342.

Johnson, K.T.M., and Dick, H.J.B., 1992, Open system melting and temporal and spatial variation of peridotite and basalt at the Atlantis II fracture zone: Journal of Geophysical Research, v. 97, p. 9219–9241, doi: 10.1029/92JB00701.

Kelemen, P.B., Yogodzinski, G.M., and Scholl, D.W., 2004, Along-strike variation in the aleutian island arc: Genesis of high Mg# andesite and implications for continental crust: Geophysical Monograph Series, v. 138, p. 223–276, doi: 10.1029/138GM11.

Kelley, D.S., Karson, J.A., Blackman, D.K., Früh-Green, G.L., Butterfield, D.A., Lilley, M.D., Olson, E.J., Schrenk, M.O., Roe, K.K., Lebon, G.T., Rivizzigno, P., and Party, the A.-60 S., 2001, An off-axis hydrothermal vent field near the Mid-Atlantic Ridge at 30° N: Nature, v. 412, p. 145–149, doi: 10.1038/35084000.

Kinzler, R.J., 2006, Melting of Mantle Peridotite at Pressures Approaching the Spinel to Garnet Transition: Mineralogical Magazine, v. 58A, p. 483–484, doi: 10.1180/minmag.1994.58a.1.251.

Klein, E.M., and Langmuir, C.H., 1987, Global correlation of ocean ridge basalt chemistry with axial depth and crustal thickness: Journal of Geophysical Research, v. 92, p. 8089–8115, doi: 10.1029/JB092iB08p08089.

Klein, E.M., and Langmuir, C.H., 1989, Local Versus Global in Ocean Ridge Basalt

Chemistry: Journal of Geophysical Research, v. 94, p. 4241–4252.

Kogiso, T., Hirschmann, M., and Reiners, P., 2004, Length scales of mantle heterogeneities and their relationship to ocean island basalt geochemistry: v. 68, p. 345–360, doi: 10.1016/S0016-7037(03)00419-8.

Komiya, T., Maruyama, S., Hirata, T., and Yurimoto, H., 2002, Petrology and Geochemistry of MORB and OIB in the Mid-Archean North Pole Region, Pilbara Craton, Western Australia: Implications for the Composition and Temperature of the Upper Mantle at 3.5 Ga: International Geology Review, v. 44, p. 988–1016, doi: https://doi.org/10.2747/0020-6814.44.11.988.

Komiya, T., Maruyama, S., Hirata, T., Yurimoto, H., and Nohba, S., 2004, Geochemistry of the oldest MORB and OIB in the Isua Supracrustal Belt, southern West Greenland: Implications for the composition and temperature of early Archean upper mantle: The Island Arc, v. 13, p. 47–72, doi: https://doi.org/10.1111/j.1440-1738.2003.00416.x.

Kong, L.S.L., Solomon, S.C., and Purdy, G.M., 1992, Microearthquake characteristics of a mid-ocean ridge along-axis high: Journal of Geophysical Research, v. 97, p. 1659–1685, doi: 10.1029/91JB02566.

Koornneef, J.M., Stracke, A., Bourdon, B., and Grönvold, K., 2012, The influence of source heterogeneity on the U-Th-Pa-Ra disequilibria in post-glacial tholeiites from Iceland: Geochimica et Cosmochimica Acta, v. 87, p. 243–266, doi: 10.1016/j.gca.2012.03.041.

Kransnov, S.G., Cherkashev, G.A., Stepanova, T., Batuyev, B.N., Krotov, A.G., Malin, B.V., Maslov, M.., Markov, V.F., Poroshina, I.M., Samovarov, M., Ashadze, A.M., Lazareva, L., and Ermolayev, I.., 1994, Detailed geological studies of hydrothermal fields in the North Atlantic: Geological Society, London, Special Publications, v. 87, p. 43–64, doi: 10.1144/GSL.SP.1995.087.01.05.

Kuritani, T., Kitagawa, H., and Nakamura, E., 2005, Assimilation and fractional

crystallization controlled by transport process of crustal melt: Implications from an alkali basalt-dacite suite from Rishiri Volcano, Japan: Journal of Petrology, v. 46, p. 1421–1442, doi: 10.1093/petrology/egi021.

Kvassnes, A., and Sweetman, A.J., 2004, The evolution of oceanic gabbros : in-situ and ancient examples: Phd ,MIT — Woods Hole Joint Program in Oceanography, doi: 10.1575/1912/1860.

Lambart, S., Backer, M., and Stolper, E., 2016, The role of pyroxenite in basalt genesis: Melt-PX, a melting parameterization of mantle pyroxenites between 0.9 to 5 GPa: Journal of Geophysical Research: Solid Earth, v. 121, p. 5708–5735, doi: 10.1002/ 2015JB012762.

Lambart, S., Laporte, D., and Schiano, P., 2009, An experimental study of pyroxenite partial melts at 1 and 1.5 GPa: Implications for the major-element composition of Mid-Ocean Ridge Basalts: Earth and Planetary Science Letters, v. 288, p. 335–347, doi: 10.1016/j.epsl.2009.09.038.

Langmuir, C.H., 1989, Geochemical consequences of in situ crystallization: Nature, v. 340, p. 199–205, doi: 10.1038/340199a0.

Langmuir, C., and Hanson, G., 1980, An evaluation of major element heterogeneity in the mantle sources of basalts: Philos. Trans. of the Royal Society London, v. A297, p. 383–407.

Langmuir, H., Klein, E.M., and Plank, T., 1992, Petrological Systematics of Mid-Ocean Ridge Basalts : Constraints on Melt Generation Beneath Ocean Ridges:Geophysical Monograph Series, v. 71, doi: https://doi.org/10.1029/GM071p0183

Lee, C.-T.A., and Chin, E.., 2014, Calculating melting temperatures and pressures of peridotite protoliths: Implications for the origin of cratonic mantle: Earth and Planetary Science Letters, v. 403, p. 273–286, doi: https://doi.org/10.1016/j.epsl.2014.06.048.

Lissenberg, C.J., and Dick, H.J.B., 2008, Melt-rock reaction in the lower oceanic crust

and its implications for the genesis of mid-ocean ridge basalt: Earth and Planetary Science Letters, v. 271, p. 311–325, doi: 10.1016/j.epsl.2008.04.023.

Lister, C.R.B., 1974, On the Penetration of Water into Hot Rock: Geophysical Journal of the Royal Astronomical Society, v. 39, p. 465–509, doi: 10.1111/j.1365-246X.1974.tb05468.x.

Liu, B., and Liang, Y., 2017, Supplementary Materials for The prevalence of kilometer-scale heterogeneity in the source region of: Science Advances, v. 3, p. 1–8, doi: DOI: 10.1126/sciadv.1701872.

Lyubetskaya, T., and Korenaga, J., 2007, Chemical composition of Earth's primitive mantle and its variance: 1. Method and results: Journal of Geophysical Research: Solid Earth, v. 112, p. 1–21, doi: 10.1029/2005JB004223.

Macdonald, K.C., Fox, P.J., Perram, L.J., Eisen, M.F., Haymon, R.M., Miller, S.P., Carbotte, S.M., Cormier, M.H., and Shor, A.N., 1988, A new view of the mid-ocean ridge from the behaviour of ridge-axis discontinuities: Nature, v. 335, p. 217–225, doi: 10.1038/335217a0.

MacLeod, C.J., Searle, R.C., Murton, B.J., Casey, J.F., Mallows, C., Unsworth, S.C., Achenbach, K.L., and Harris, M., 2009, Life cycle of oceanic core complexes: Earth and Planetary Science Letters, v. 287, p. 333–344, doi: https://doi.org/10.1016/j.epsl.2009.08.016.

de Martin, B.J., Reves-Sohn, R.A., Canales, J.P., and Humphris, S.E., 2007, Kinematics and geometry of active detachment faulting beneath the Trans-Atlantic geotraverse (TAG) hydrothermal field on the Mid-Atlantic Ridge: Geology, v. 35, p. 711–714, doi: 10.1130/G23718A.1.

McKenzie, D., Stracke, A., Blichert-Toft, J., Albarède, F., and Grönvold, K., 2004, Source enrichment processes responsible for isotopic anomalies in oceanic island basalts: Geochimica et Cosmochimica Acta, v. 68, p. 2699–2724, doi: https://doi.org/10.1016/j.gca.2003.10.029.

Meibom, A., and Anderson, D.L., 2004, The statistical upper mantle assemblage: Earth and Planetary Science Letters, v. 217, p. 123–139, doi: https://doi.org/10.1016/S0012-821X(03)00573-9.

Müller, R.D., Sdrolias, M., Gaina, C., and Roest, W.R., 2008, Age, spreading rates, and spreading asymmetry of the world's ocean crust: Geochemistry, Geophysics, Geosystems, v. 9, p. 1–19, doi: 10.1029/2007GC001743.

Murton, B.J., and Rona, P.A., 2015, Carlsberg Ridge and Mid-Atlantic Ridge: Comparison of slow spreading centre analogues: Deep-Sea Research Part II: Topical Studies in Oceanography, v. 121, p. 71–84, doi: 10.1016/j.dsr2.2015.04.021.

Niu, Y., and Batiza, R., 1997, Trace element evidence from seamounts for recycled oceanic crust in the Eastern Pacific mantle: Earth and Planetary Science Letters, v. 148, p. 471–483.

Niu, Y., and Hékinian, R., 1997, Spreading-rate dependence of the extent of mantle melting beneath ocean ridges: Nature, v. 385, p. 326–328, doi: 10.1038/385326a0.

Niu, Y., Regelous, M., Wendt, I.J., Batiza, R., and O'Hara, M.J., 2002, Geochemistry of near-EPR seamounts: importance of source vs. process and the origin of enriched mantle component: Earth and Planetary Science Letters, v. 199, p. 327–345, doi: https://doi.org/10.1016/S0012-821X(02)00591-5.

Niu Y., 1997, Mantle Melting and Melt Extraction Processes beneath Ocean Ridges: Evidence from Abyssal Peridotites: Journal of Petrology, v. 38, p. 1047–1074.

Olive, J.A., and Escartín, J., 2016, Dependence of seismic coupling on normal fault style along the Northern Mid-Atlantic Ridge: Geochemistry, Geophysics, Geosystems, v. 17, p. 4128–4152, doi: 10.1002/2016GC006460.

Paquet, M., Cannat, M., Brunelli, D., Hamelin, C., and Humler, E., 2016, Effect of melt/mantle interactions on MORB chemistry at the easternmost Southwest Indian Ridge (61 to 67°E): Geochemistry Geophysics Geosystems, v. 17, p. 4605–4640, doi: 10.1002/2016GC006385.

Patiño Douce, A.E., 1997, Generation of metaluminous A-type granites by low-pressure melting of calc-alkaline granitoids: Geology, v. 25, p. 743–746, doi: 10.1130/0091-7613(1997)025<0743:GOMATG>2.3.CO;2.

Petermann, M., and Hirschmann, M.., 2002, Trace-element partitioning between vacancy-rich eclogitic clinopyroxene and silicate melt: American Mineralogist, v. 87, p. 1365–1376, doi: https://doi.org/10.2138/am-2002-1012.

Pietruszka, A.J., Norman, M.D., Garcia, M.O., Marske, J.P., and Burns, D.H., 2013, Chemical heterogeneity in the Hawaiian mantle plume from the alteration and dehydration of recycled oceanic crust: Earth and Planetary Science Letters, v. 361, p. 298–309, doi: 10.1016/j.epsl.2012.10.030.

Planert, L., Flueh, E.R., Tilmann, F., Grevemeyer, I., and Reston, T.J., 2010, Crustal structure of a rifted oceanic core complex and its conjugate side at the MAR at 5°S: Implications for melt extraction during detachment faulting and core complex formation: Geophysical Journal International, v. 181, p. 113–126, doi: 10.1111/j.1365-246X.2010.04504.x.

Plank, T., and Langmuir, C.H., 2008, Effects of the melting regime on the composition of the oceanic crust: Journal of Geophysical Research, v. 97, p. 19749, doi: 10.1029/92jb01769.

Presnall, D.C., Dixon, S.A., Dixon, J.R., O'Donnell, T.., Brenner, N.L., Schrock, R.L., and Dycus, D.W., 1978, Liquidus phase relations on the join diopside-forsterite-anorthite from 1 atm to 20 kbar: Their bearing on the generation and crystallization of basaltic magma: Contributions to Mineralogy and Petrology, v. 66, p. 203–220, doi: https://doi.org/10.1007/BF00372159.

Prytulak, J., and Elliott, T., 2009, Determining melt productivity of mantle sources from238U-230Th and235U-231Pa disequilibria; an example from Pico Island, Azores: Geochimica et Cosmochimica Acta, v. 73, p. 2103–2122, doi: 10.1016/j.gca.2009.01.001.

Prytulak, J., and Elliott, T., 2007, TiO2 enrichment in ocean island basalts: Earth and Planetary Science Letters, v. 263, p. 388–403, doi: 10.1016/j.epsl.2007.09.015.

Putirka, K.D., Perfit, M.., Ryerson, F.J., and Jackson, M.G., 2007, Ambient and excess mantle temperatures, olivine thermometry, and active vs. passive upwelling: Chemical Geology, v. 241, p. 177–206, doi: https://doi.org/10.1016/j.chemgeo.2007.01.014.

Rona, P.A., Thompson, G., Mottl, M.J., Karson, J.A., Jenkins, W.J., Graham, D., Von Damm, K., and Edmond, J.M., 1984, Hydrothermal activity at the Trans-Atlantic Geothermal Field, Mid-Atlantic ridge crest at 26°N: Journal of Geophysical Research, v. 89, p. 11365–11377, doi: 10.1029/JB089iB13p11365.

Le Roux, L.J., Glendenin, L.E., 1963, Half-life of ^{232}Th: Proceedings of National Meeting on Nuclear Energy, p. 83–94.

Rudge, J.F., Maclennan, J., and Stracke, A., 2013, The geochemical consequences of mixing melts from a heterogeneous mantle: Geochimica et Cosmochimica Acta, v. 114, p. 112–143, doi: 10.1016/j.gca.2013.03.042.

Salters, V.J.M., and Stracke, A., 2004, Composition of the depleted mantle: Geochemistry, Geophysics, Geosystems, v. 5, doi: 10.1029/2003GC000597.

Sandwell, D.T., and Smith, W.H.F., 2009, Global marine gravity from retracked Geosat and ERS-1 altimetry: Ridge segmentation versus spreading rate: Journal of Geophysical Research: Solid Earth, v. 114, p. 1–18, doi: 10.1029/2008JB006008.

Saunders, A.D., Norry, M.J., and Tarney, J., 1988, Origin of MORB and Chemically-Depleted Mantle Reservoirs: Trace Element Constraints: Journal of Petrology, v. Special_Vo, p. 415–455, doi: https://doi.org/10.1093/petrology/Special_Volume.1.415.

Schilling, J.-G., 1973, Iceland Mantle Plume: Geochemical Study of Reykjanes Ridge: v. 242, 565–571 p., doi: 10.1038/242565a0.

Scotti, D.R., and Stevenson, J., 1989, A Self-Consistent Model of :NIelting, Magma

Migration and Buoyancy-Driven Circulation Beneath Mid-Ocean Ridges: J.\ Geophys.\ Res., v. 94, p. 2973–2988.

Sims, K.W.W., Gill, J.B., Dosseto, A., Hoffmann, D.L., Lundstrom, C.C., Williams, R.W., Ball, L., Tollstrup, D., Turner, S., Prytulak, J., Glessner, J.J.G., Standish, J.J., and Elliott, T., 2008, An inter-laboratory assessment of the thorium isotopic composition of synthetic and rock reference materials: Geostandards and Geoanalytical Research, v. 32, p. 65–91, doi: 10.1111/j.1751-908X.2008.00870.x.

Sims, K.W.W., Hart, S.R., Reagan, M.K., Blusztajn, J., Staudigel, H., Sohn, R.A., Layne, G.D., Ball, L.A., and Andrews, J., 2008, ^{238}U-^{230}Th-^{226}Ra-^{210}Pb-^{210}Po,^{232}Th-^{228}Ra, and ^{235}U-^{231}Pa constraints on the ages and petrogenesis of Vailulu'u and Malumalu lavas, Samoa: Geochemistry, Geophysics, Geosystems, v. 9, doi: 10.1029/2007GC001651.

Smith, D.K., Cann, J.R., and Escartín, J., 2006, Widespread active detachment faulting and core complex formation near 13° N on the Mid-Atlantic Ridge: Nature, v. 442, p. 440–443, doi: 10.1038/nature04950.

Smith, D.K., Escartín, J., Schouten, H., and Cann, J.R., 2008, Fault rotation and core complex formation: Significant processes in seafloor formation at slow-spreading mid-ocean ridges (Mid-Atlantic Ridge, 13°-15°N): Geochemistry, Geophysics, Geosystems, v. 9, doi: 10.1029/2007GC001699.

Spencer, S., Smith, D.K., Cann, J.R., Lin, J., and McAllister, E., 1997, Structure and Stability of Non-Transform Discontinuities on the Mid-Atlantic Ridge between 24° N and 30° N: Marine Geophysical Research, v. 19, p. 339–362, doi: 10.1023/A:1004200411959.

Standish, J.J., Dick, H.J.B., Michael, P.J., Melson, W.G., and O'Hearn, T., 2008, MORB generation beneath the ultraslow spreading Southwest Indian Ridge (9-25°E): Major element chemistry and the importance of process versus source: Geochemistry, Geophysics, Geosystems, v. 9, doi: 10.1029/2008GC001959.

Stracke, A., and Bourdon, B., 2009, The importance of melt extraction for tracing mantle heterogeneity: Geochimica et Cosmochimica Acta, v. 73, p. 218–238, doi: 10.1016/j.gca.2008.10.015.

Sun, S. -s., and McDonough, W.F., 1989, Chemical and isotopic systematics of oceanic basalts: implications for mantle composition and processes: Geological Society, London, Special Publications, v. 42, p. 313–345, doi: 10.1144/GSL.SP.1989.042.01.19.

Tivey, M.A., Schouten, H., and Kleinrock, M.C., 2003, A near-bottom magnetic survey of the Mid-Atlantic Ridge axis at 26°N: Implications for the tectonic evolution of the TAG segment: Journal of Geophysical Research: Solid Earth, v. 108, p. 1–13, doi: 10.1029/2002JB001967.

Tucholke, B.E., Behn, M.D., Buck, W.R., and Lin, J., 2008, Role of melt supply in oceanic detachment faulting and formation of megamullions: Geology, v. 36, p. 455–458, doi: https://doi.org/10.1130/G24639A.1.

Tucholke, B.E., and Lin, J., 1994, A geological model for the structure of ridge segments in slow spreading ocean crust: Journal of Geophysical Research: Solid Earth, v. 99, p. 11937–11958, doi: https://doi.org/10.1029/94JB00338.

Tucholke, B.E., Lin, J., and Kleinrock, M.C., 1998, Megamullions and mullion structure defining oceanic metamorphic core complexes on the Mid-Atlantic Ridge: Journal of Geophysical Research: Solid Earth, v. 103, p. 9857–9866, doi: 10.1029/98JB00167.

Wanless, V.D., and Shaw, A.M., 2012, Lower crustal crystallization and melt evolution at mid-ocean ridges: Nature Geoscience, v. 5, p. 651, https://doi.org/10.1038/ngeo1552.

Waters, C.L., Sims, K.W.W., Perfit, M.R., Blichert-Toft, J., and Blusztajn, J., 2011, Perspective on the genesis of E-MORB from chemical and isotopic heterogeneity at 9-10°n East Pacific Rise: Journal of Petrology, v. 52, p. 565–602, doi:

10.1093/petrology/egq091.

White, W.M., and Klein, E.M., 2013, Composition of the Oceanic Crust: Elsevier Ltd., v. 4, 457–496 p., doi: 10.1016/B978-0-08-095975-7.00315-6.

White, W., and Schilling, J.-G., 1978, The nature and origin of geochemical variation in Mid-Atlantic Ridge basalts from the Central North Atlantic: v. 42, 1501–1516 p., doi: 10.1016/0016-7037(78)90021-2.

Wilson, S.C., Murton, B.J., and Taylor, R.N., 2013, Mantle composition controls the development of an Oceanic Core Complex: Geochemistry, Geophysics, Geosystems, v. 14, p. 979–995, doi: 10.1002/ggge.20046.

Woodhead, J.D., 1989, Geochemistry of the Mariana arc (western Pacific): Source composition and processes: Chemical Geology, v. 76, p. 1–24, doi: https://doi.org/10.1016/0009-2541(89)90124-1.

Workman, R.K., and Hart, S.R., 2005, Major and trace element composition of the depleted MORB mantle (DMM): Earth and Planetary Science Letters, v. 231, p. 53–72, doi: 10.1016/j.epsl.2004.12.005.

Xu, M., Canales, J.P., Tucholke, B.E., and DuBois, D.L., 2009, Heterogeneous seismic velocity structure of the upper lithosphere at Kane oceanic core complex, Mid-Atlantic Ridge: Geochemistry, Geophysics, Geosystems, v. 10, doi: 10.1029/2009GC002586.

Yu, Z., Li, J., Liang, Y., Han, X., Zhang, J., and Zhu, L., 2013, Distribution of large-scale detachment faults on mid-ocean ridges in relation to spreading rates: Acta Oceanologica Sinica, v. 32, p. 109–117, doi: 10.1007/s13131-013-0397-y.

Zindler, A., and Hart, S.R., 1986, Chemical Geodynamics: Annual Review of Earth and Planetary Sciences, v. 14, p. 493–571, doi: 10.1146/annurev.earth.14.1.493.

Zonenshain, L.P., Kuzmin, M.I., Lisitsin, A.P., Bogdanov, Y.A., and Baranov, B.V., 1989, Tectonics of the Mid-Atlantic rift valley between the TAG and MARK areas (26–24°N): Evidence for vertical tectonism: Tectonophysics, v. 159, p. 1–23, doi:

https://doi.org/10.1016/0040-1951(89)90167-4.

Zou, H., 2010, Batch Melting: Quantitative Geochemistry, p. 1–22, doi: 10.1142/9781860948206_0001.

Appendix A

Batch melting model

Zou (2010) states that in the batch melting model, liquid melts are assumed to stay in equilibrium with the residual solid throughout the entire melting process. In this model, the mass porosity (ψ) is always equal to the amount of melt extracted, the ratio of liquid to the original solid reservoir (X) is 0 before partial melting starts and then equals to the degree of partial melting (F) after partial melting starts. An important precondition of any time-independent model is that D_i/F must be close to or greater than 1 (Bourdon et al., 2003), where D_i is the mineral/melt partition coefficient for an element i. Therefore, the F values for batch melting model must be very small, since the D values for nuclides in question in mantle minerals are also small (Blundy and Wood, 2003). The fundamental equation for batch melting model is:

$$C_L = \frac{C_o}{D_o + F\,(1 - D_o)}$$

Where C_L equals to the concentration of an element in extracted melts; C_o equals to the initial concentration of this element in the source; D equals to the bulk partition coefficient of this element.